Published on 22 January 2026. Downloaded by University of California - Los Angeles on 1/28/2026 4:59:03 PM.

NJC

ROYAL SOCIETY OF CHEMISTRY

PAPER

View Article Online
View Journal

Check for updates

Cite this: DOI: 10.1039/d5nj04475h

Development of a sustainable and recyclable oxC$_{60}$–Ly@Fe GCE electrode: an eco-friendly catalyst for electrochemical sulfonation to synthesize benzenesulfonic acids

Karkaz Thalij,[a] Ebraheem Abdu Musad Saleh,[b] Amer Alhaj Zen,[c] Mohammed B. Alqaraguly,[d] Abdulrahman A. Almehizia,[*e] Erkabay Eshchanov,[f] Bekzod Madaminov,[g] Zokir Ataullaev,[h] Yuldash Rajabovich Takhirov,[i] Elyor Berdimurodov,[jkl] Khasan Berdimuradov[mn] and Rasulbek Eshmetov[o]

Received 16th November 2025,
Accepted 4th January 2026

DOI: 10.1039/d5nj04475h

rsc.li/njc

In this study a reusable and environmentally benign catalyst, oxC$_{60}$–Ly@Fe, was rationally designed and synthesized. The catalyst's efficacy and performance were systematically evaluated in the electrosynthesis of chlorobenzenes **1(a-l)** and S_8 **2(a)** derivatives, enabling the synthesis of benzenesulfonic acid derivatives **3(a–i)** under mild reaction conditions, specifically at ambient temperature, a current density of 15 mA, and a reaction time of 1 hour, with urea/ChCl serving as the electrolyte. This electrochemical process afforded excellent product yields ranging from 87% to 95%. Key electrochemical catalytic metrics, including the *E*-factor, atom economy, turnover number (TON), and turnover frequency (TOF), were calculated, demonstrating the process's environmental compatibility and superior catalytic performance. The catalyst is thoroughly characterized (FT-IR, XRD, SEM, EDX/EDS, TGA, XPS, CV, BET), and the products are confirmed by melting point, NMR, and CHN analyses.

Introduction

Sulfonation is extensively applied across various industrial sectors due to its crucial role; however, conventional sulfonation synthesis approaches suffer from drawbacks including elevated reaction temperatures, extended reaction durations, low product yields, poor compliance with green chemistry protocols, and suboptimal atom economy. Sulfonation reactions are highly important in pharmaceutical chemistry because they introduce sulfonic acid groups (–SO_3H) into drug molecules, significantly enhancing their water solubility, bioavailability, and biological activity.[1,2] Many drugs face challenges such as poor solubility and slow absorption, which limit their therapeutic effectiveness; sulfonation can overcome these issues by making molecules more hydrophilic and thus easier to absorb in the body.[3,4] Furthermore, sulfonated compounds often serve as key intermediates or active pharmaceutical ingredients (APIs) in various medications. Pharmaceutical drugs based on sulfonic acid

[a] Food Science Department, Tikrit University, Iraq. E-mail: kthalij@tu.edu.iq
[b] Department of Chemistry, College of Science and Humanities in Al-Kharj, Prince Sattam Bin Abdulaziz University, Al-Kharj, 11942, Saudi Arabia. E-mail: eb.saleh@psau.edu.sa
[c] Chemistry & Forensics Department, Nottingham Trent University, Clifton Camus, Nottingham, Ng118NS, UK. E-mail: amer.alhajzen@ntu.ac.uk
[d] Medical laboratories techniques, Hilla university college, Babylon, Iraq. E-mail: mohammed9basim@gmail.com
[e] Drug Exploration and Development Chair (DEDC), Department of Pharmaceutical Chemistry, College of Pharmacy, King Saud University, Riyadh 11451, Saudi Arabia. E-mail: mehizia@ksu.edu.sa
[f] Department of Chemistry, Urgench State University, Urgench, Uzbekistan. E-mail: erkabay.e@urdu.uz
[g] Department of General Professional Sciences, Mamun University, Urgench, Uzbekistan. E-mail: madaminov_bekzod@mamunedu.uz
[h] Natural Science Department, Urganch State Pedagogical Institute, Urgench, Uzbekistan. E-mail: zokirjon16081987@gmail.com
[i] Department of Chemistry, Urgench State University named after Abu Rayhan Biruni, 220100 Urgench, Uzbekistan. E-mail: yuldash_78@mail.ru, y.taxirov@gmail.com
[j] Faculty of Chemistry, National University of Uzbekistan, Tashkent, 100034, Uzbekistan
[k] University of Tashkent for Applied Sciences, Str. Gavhar 1, Tashkent, 100149, Uzbekistan
[l] School of Medicine, Central Asian University, Tashkent, 111221, Uzbekistan. E-mail: elyor170690@gmail.com
[m] Shahrisabz Faculty of Food Engineering, Karshi State Technical University, Karshi, Uzbekistan
[n] Chemistry, Azerbaijan State Oil and Industry University, Baku, Azerbaijan. E-mail: berdimuradovkhasan196@gmail.com
[o] Natural sciences, Ma'mun Universiteti, Urgench, Uzbekistan. E-mail: rasulbekeshmetov4@gmail.com

Published on 22 January 2026. Downloaded by University of California - Los Angeles on 1/28/2026 4:59:03 PM.

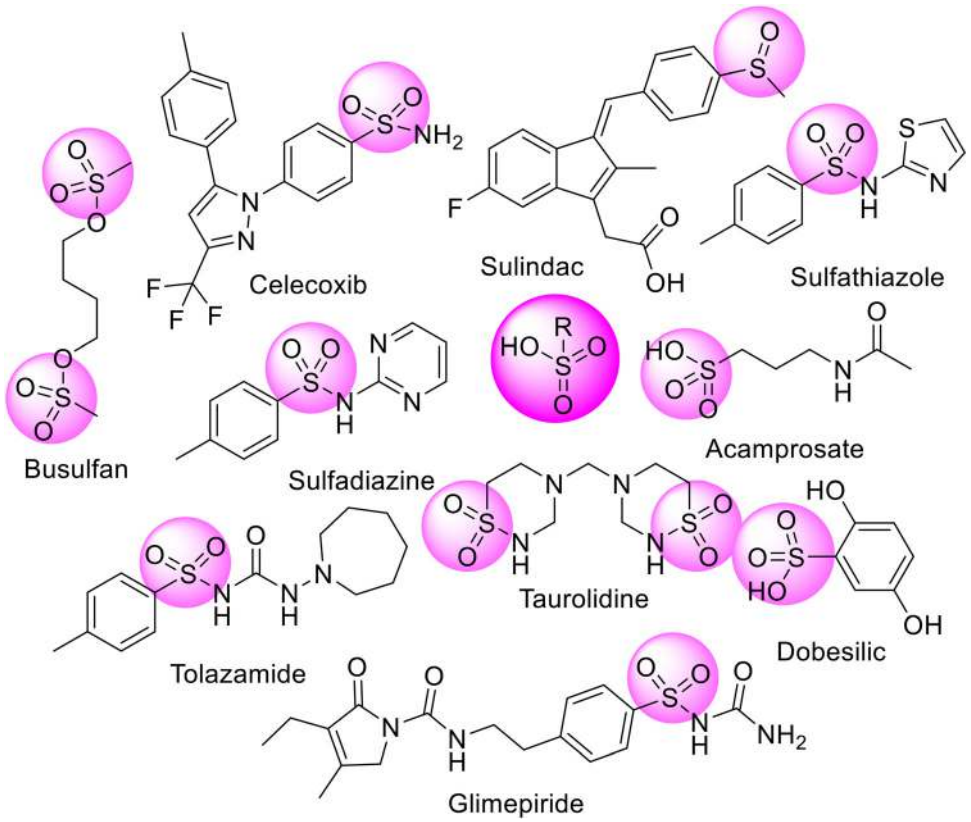


Fig. 1 Market introduction of sulfonation-synthesized drugs.

include celecoxib (anti-inflammatory),[5] sulindac (anti-inflammatory),[6] sulfathiazole (antimicrobial),[7] busulfan (anti-cancer),[8] sulfadiazine (anti-infection),[9] acamprosate (high blood pressure),[10] tolazamide (diabete),[11] taurolidine (antimicrobial),[8,12] dobesilic acid (hemorrhoid),[13] and glimepiride (high blood sugar)[10,14] (Fig. 1).

Numerous methodologies for the synthesis of aryl sulfonic acids have been reported in the literature,[15,16] and their representative results are summarized in Table 1. As shown, sulfonation has been carried out using reagents such as $K_2S_2O_5$, $NaHSO_3$, H_2SO_4, trifluoroacetylsulfuric acid, and $ClSO_3H$. However, these conventional procedures suffer from several drawbacks, including the requirement for elevated temperatures, prolonged reaction times, and high pressures, as well as the use of hazardous, corrosive, and toxic reagents. These limitations not only pose significant environmental and safety concerns but also contradict the principles of green chemistry and create substantial barriers to the commercialization of such methods. Accordingly, the development of a simple, green, reusable electrocatalytic system with high atom economy, scalability, and potential for industrial commercialization is of great importance.

Electrosynthesis plays a crucial role in green chemistry and organic synthesis by providing a sustainable and environmentally friendly alternative to traditional chemical methods.[24,25] It uses electricity as a clean reagent to drive redox reactions, eliminating the need for hazardous chemical oxidants or reductants and reducing the generation of toxic waste.[26,27] Electrosynthesis allows for precise control of reaction conditions, such as voltage and current, enabling selective transformations under mild conditions, often at ambient temperature and pressure.[28,29] This approach improves energy efficiency, enhances atom economy, and supports the use of greener solvents or even solvent-free reactions.[30,31] Moreover, electrosynthesis enables access to complex organic molecules and functionalized intermediates that are valuable in pharmaceuticals and fine chemicals,

Table 1 Comparative investigation of organic synthetic routes to sulfonic derivatives

Entry	Catalyst	Reagent	Solvent	Conditions	Year	Yield %
1	Mn	$K_2S_2O_5$	DCM	r.t., 4 h	2023	94[17]
2	Pyridinium dichromate	$NaHSO_3$	—	100 °C, 1500 Torr, 10 min,	2020	85[18]
3	—	H_2SO_4	—	80 °C, 0.5 h	2014	80[19]
4	—	Triflic acid	H_2O	20 °C, 1 h	2021	90[20]
5	—	H_2SO_4	—	95 °C, 12 h	2022	99[21]
6	—	$ClSO_3H$	DCE	0 °C, 0.5 h	2013	95[22]
7	—	$ClSO_3H$	DCE	r.t., 12 h	2017	90[23]

 This journal is © The Royal Society of Chemistry and the Centre National de la Recherche Scientifique 2026

Published on 22 January 2026. Downloaded by University of California - Los Angeles on 1/28/2026 4:59:03 PM.

while also aligning with several green chemistry principles like waste prevention, safer chemical synthesis, and energy conservation.[32] Its scalability and adaptability to continuous-flow processes further underscore its potential for sustainable industrial applications.[33,34]

To address these limitations and streamline the sulfonation process, an electrode composed of oxC$_{60}$–Ly@Fe GCE, based on an inexpensive and readily available metal, was designed and synthesized. The catalytic performance of this electrode was investigated in the electro-sulfonation of chlorobenzene derivatives **1(a–p)** in the presence of S_8 **2(a)**, as well as in the synthesis of a series of benzenesulfonic acid derivatives **3(a–p)** with good to excellent yield 87–95%. Reactions were conducted under optimized conditions, including ambient temperature, atmospheric pressure, a reaction time of 1 hour, and a constant current of 15 mA, utilizing a urea/ChCl DES as the reaction medium. The primary objective of this work was to develop a cost-effective and accessible iron-based electrode, modified with oxC$_{60}$ to enhance the catalyst surface area. This catalyst not only demonstrated high catalytic efficiency but also exhibited recyclability, reusability, environmental friendliness, and a superior atom economy, thereby highlighting its potential for sustainable electrocatalytic applications.

Material, methods and equipment

All chemicals and materials used in this study, including choline chloride (ChCl), urea, fullerene (C$_{60}$), nitric acid (80%), potassium permanganate, hydrogen peroxide (25%), chlorobenzenes **1(a–l)**, sulfur, silica gel, silver nitrate, iron trichloride, L-lysine, sulfuric acid (98%), hydrochloric acid, sodium chloride, sodium bromide, and potassium chromate, and organic solvents were obtained in analytical grade and used as received without any further purification. The following equipment was employed in this study: an SB162 model heat stirrer, a RE100-Pro LCD rotary vacuum evaporator, a Buchi B545 melting point apparatus, and a Pars Azma drying oven. Catalyst characterization involved several instrumental techniques: functional groups were identified using FT-IR spectroscopy (ALPHA II FTIR, Bruker), crystalline structures were determined by X-ray diffraction (Bruker D8 XRD), surface morphology was examined *via* scanning electron microscopy (SEM), and elemental compositions were analyzed through energy-dispersive X-ray spectroscopy (EDX/EDS) using the SU8600 microscope. Thermal stability was assessed by thermogravimetric analysis (TGA; Lr-TGA), while X-ray photoelectron spectroscopy (XPS; AXIS Supra) provided information on bonding types and chemical states. Electrochemical properties of the electrodes were evaluated by cyclic voltammetry (CV), and porosity and surface area were measured using the BET technique (V-Sorb 2800TP). The synthesized benzenesulfonic acid derivatives **3(a–p)** were structurally confirmed by ^{1}H NMR, ^{13}C NMR (Bruker 400 MHz), and elemental analysis (CHN; EMA 502) (Fig. 2).

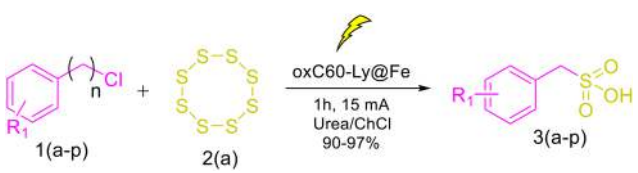


Fig. 2 Electro-organic synthesis of benzenesulfonic acids **3(a–p)**.

Procedure for synthesis of urea/ChCl DES

To synthesize urea/choline chloride (ChCl) DES, urea and ChCl are combined in a 2 : 1 molar ratio (typically 50 g urea to 25 g ChCl) and placed in a clean, dry 200 mL round-bottom flask equipped with a heater stirrer and a magnetic bar. The mixture is gently heated to 70 °C with continuous stirring. Heating and mixing are maintained until the solids are fully melted and a homogeneous, transparent liquid forms, which generally requires about 60 minutes. Care should be taken not to exceed 100 °C to prevent decomposition. Upon complete dissolution and homogenization, the resulting DES is allowed to cool to room temperature, with stirring continued until a stable liquid is obtained. The synthesized urea/ChCl DES should be stored in a tightly sealed container to prevent moisture uptake, as H_2O can affect its physical and chemical properties. The final product is a clear and viscous liquid (Fig. 3).[35]

Functionalized fullerene to oxC$_{60}$ using modified Hummers' method

Fullerene oxide was prepared using a refined Hummers' method, employing fullerene powder as the precursor, as illustrated in Fig. 4. Initially, 3.0 g of fullerene powder (particle size <40 μm, Sigma-Aldrich) was introduced into a two-necked 100 mL flask equipped with a mechanical stirrer. To this, 90 mL of concentrated H_2SO_4 was carefully added, and the suspension was stirred continuously for 1 hour under a fume hood to ensure proper dispersion and activation of the fullerene surface.

Following this, 30 mL of concentrated HNO_3 (80%), known for its oxidizing and gas-evolving properties, was gradually incorporated dropwise into the reaction mixture while maintaining vigorous stirring and an ice-water bath to control the

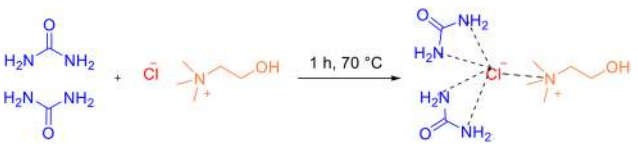


Fig. 3 Synthesis of urea/ChCl DES.

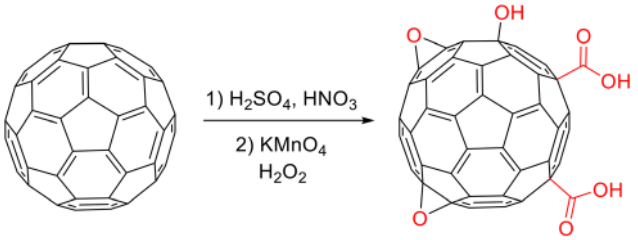


Fig. 4 Oxidation of fullerene to oxC$_{60}$.

Published on 22 January 2026. Downloaded by University of California - Los Angeles on 1/28/2026 4:59:03 PM.

exothermic reaction and avoid overheating. Once the temperature was stabilized at approximately 8 °C, 13 g of $KMnO_4$ was slowly added in small portions under continuous stirring and ice cooling to facilitate controlled oxidation of fullerene for 2.5 hours at ambient temperature, with the reaction proceeding inside the fume hood to safely vent gases and vapors. The mixture was then carefully diluted by adding 400 mL of deionized H_2O dropwise, preventing excessive heating or violent reactions, followed by 1.5 hours of stirring at room temperature to complete the oxidation stage. Subsequently, 17 mL of 25% H_2O_2 solution was introduced, which rapidly reduced the manganese species, transforming the dark suspension into a yellow, frothy solution indicative of fullerene oxide (oxC_{60}) formation. After decanting the supernatant, the solid product was collected by filtration and subjected to sequential washing. The solid was first washed twice with 150 mL portions of deionized water to remove residual acids and manganese by-products. Then, the solid was treated with a mixture of 6 mL HCl (30%) and 6 mL of 25% H_2O_2, followed by stirring for 1 hour to further purify and remove any remaining manganese dioxide (MgO) particles. This washing and centrifugation procedure was repeated four times to ensure thorough purification. Finally, the dark solid residue was washed repeatedly with distilled water until the pH of the filtrate reached neutrality (pH ≈ 6–7), requiring approximately 200 mL of H_2O per every 10 washing cycles. The fully purified fullerene oxide (oxC_{60}) was then dried under vacuum at 70 °C for 15 hours to yield a stable, dry powder suitable for subsequent characterization and application.[36]

Procedure for synthesis of oxC_{60}–Ly@Fe

In a 250 mL two-neck round-bottom flask equipped with a condenser, magnetic stirrer, and thermometer, 200 mg of oxC_{60} and 200 mg of L-lysine were added, followed by 25 mL of toluene. The reaction mixture was heated to reflux and stirred continuously for 4 hours to promote the functionalization of oxC_{60} with L-lysine. After completion of the reaction, the mixture was allowed to cool to room temperature. The cooled mixture was then subjected to ultrasonic irradiation at a power of 300 W for 25 minutes in the presence of 150 mg of $FeCl_3$ to enhance dispersion and facilitate reaction completion. The resulting mixture was filtered under reduced pressure using vacuum filtration. The obtained solid product was washed thoroughly with hot toluene to remove organic impurities, followed by washing with warm water to eliminate any residual soluble byproducts. Finally, the purified precipitate was dried at 80 °C for 3 hours to yield the L-lysine-functionalized oxidized fullerene (oxC_{60}–Ly@Fe) as a dry powder (Fig. 5).[37]

Fabrication of oxC_{60}–Ly@Fe on GCE

For the stabilization of oxC_{60}–Ly@Fe on the GCE, the electrode surface was first thoroughly cleaned by washing with MeOH to remove any impurities or residues. Following the cleaning step, the electrode was dried at 60 °C to ensure complete removal of solvent and moisture. Subsequently, a single drop of conductive adhesive was carefully applied onto the GCE surface and evenly distributed to create a uniform adhesive layer. Then, 50 mg of oxC_{60}–Ly@Fe composite material was deposited on top of the adhesive-coated GCE and left to dry at ambient temperature for 3 hours. This protocol ensured strong adhesion and stable immobilization of the functionalized oxC_{60} composite on the GCE surface, facilitating its use in subsequent electrochemical applications (Fig. 6).

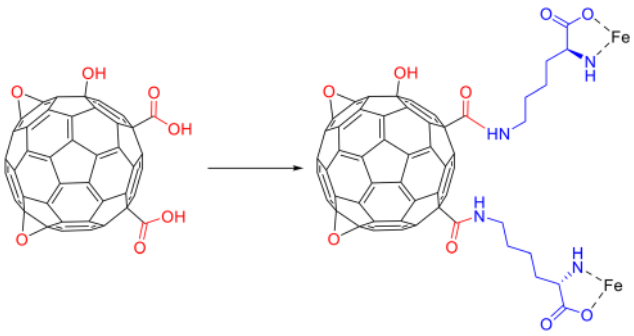


Fig. 5 Procedure for synthesis of oxC_{60}–Ly@Fe.

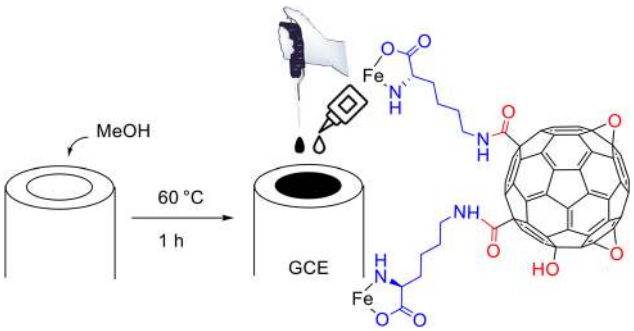


Fig. 6 Fabrication of oxC_{60}–Ly@Fe on GCE.

General procedure for electro-organic synthesis of benzenesulfonic acids 3(a–p)

A 60 mL electrolysis cell equipped with a mechanical stirrer and magnetic stir bar was charged with chlorobenzene **1(a–p)** (1 mmol), S_8 **2(a)** (1 mmol), and urea/ChCl DES (15 mL). The resulting solution was stirred at ambient temperature. Subsequently, a graphite rod anode and an oxC_{60}–Ly@Fe-modified GCE serving as the cathode were installed in the system. Electrolysis was carried out at a constant current of 15 mA using a DC power supply, with stirring maintained for 1 hour. The progress of the reaction was monitored by thin-layer chromatography (TLC) employing a 1 : 6 ethyl acetate:hexane mobile phase. Upon completion, the current was discontinued and both electrodes were removed from the mixture. To the reaction mixture, ethyl acetate (20 mL) and distilled H_2O (20 mL) were added, and the mixture was stirred at room temperature for 5 minutes. The organic and aqueous layers were separated *via* a separatory funnel. The aqueous phase, containing urea/ChCl, was collected, concentrated under reduced pressure at 70 °C using a rotary evaporator, and reserved for reuse in subsequent processes. The organic phase was treated with 1 g silica gel, concentrated under reduced pressure, and subsequently subjected to column

 This journal is © The Royal Society of Chemistry and the Centre National de la Recherche Scientifique 2026

Published on 22 January 2026. Downloaded by University of California - Los Angeles on 1/28/2026 4:59:03 PM.

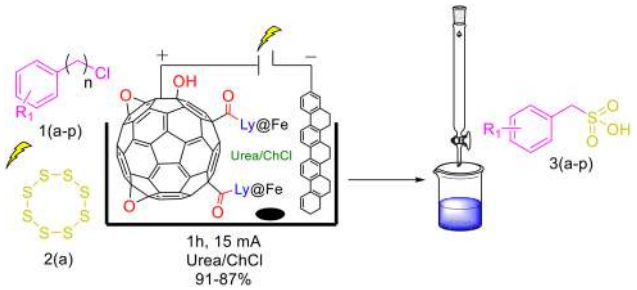


Fig. 7 Electro-organic synthesis of benzenesulfonic acids **3(a–p)**.

chromatography on silica gel (30 cm length, 2 cm diameter), employing hexane:ethyl acetate (6 : 1) as the eluent. The purified product was dried in a vacuum oven at 50 °C for 2 hours (Fig. 7).

Protocol for quantifying chlorine content employing Mohr's titrimetric analysis

To elucidate the reaction mechanism and confirm the generation of chlorine species within this electrocatalytic system, Mohr's titration was carried out using a standardized silver nitrate $AgNO_3$ solution as the titrant and K_2CrO_4 as a chromogenic indicator. An aliquot of approximately 20 mL was withdrawn from the reaction mixture after 1 hour and transferred into a clean, dry conical flask. K_2CrO_4 solution (3 mL) was then added, imparting a pale-yellow coloration that served as the visual indicator. The titration proceeded by gradual addition of the $AgNO_3$ titrant from a burette under continuous stirring to maintain homogeneity. During this process, silver ions (Ag^+) selectively precipitated chloride ions (Cl^-) as insoluble AgCl, forming a white precipitate.[38] Once all chloride ions had fully precipitated, further addition of Ag^+ ions reacted with the chromate ions to form a red-brown silver chromate (Ag_2CrO_4) precipitate. The endpoint of the titration was unequivocally signaled by a distinct color change from pale yellow to brick red, indicating total chloride ion consumption. This rigorous titrimetric analysis not only provided qualitative evidence for chlorine (Cl_2) evolution but also enabled quantitative determination of chloride concentration, thereby substantiating generation of chlorine species during the electrochemical transformation.[39]

Benzenesulfonic acid (3a). White crystal, R_f = 0.62 (4 : 1 hexane : EtOAc), yield = 94%; m.p. = 47–50 °C; ^{1}H NMR (400 MHz, D_2O): δ_H = 7.51–7.64 (m, 3H, Ar-H), 7.86 (m, 2H, Ar-H) ppm. ^{13}C NMR (100 MHz, D_2O) δ = 125.3, 129.2, 131.6, 142.4, 165.7 ppm. Anal. calcd for $C_6H_6O_3S$: C, 45.56; H, 3.82; O, 30.35; S, 20.27%. Found: C, 45.59; H, 3.79%.

4-Methoxybenzenesulfonic acid (3b). White crystal, R_f = 0.64 (4 : 1 hexane : EtOAc), yield = 97%; m.p. = 82–84 °C; ^{1}H NMR (400 MHz, D_2O): δ_H = 3.72 (s, 3H, OMe), 6.91 (dd, J = 6.9, 2.1 Hz, 2H, Ar-H), 7.63–7.65 (m, 2H, Ar-H) ppm. ^{13}C NMR (100 MHz, D_2O) δ = 55.6, 114.1, 127.2, 134.8, 161.2 ppm. Anal. calcd for $C_7H_8O_4S$: C, 44.67; H, 4.28; O, 34.00; S, 17.04%. Found: C, 44.63; H, 4.25%.

4-Methylbenzenesulfonic acid (3c). White crystal, R_f = 0.61 (4 : 1 hexane : EtOAc), yield = 95%; m.p. = 100–102 °C; ^{1}H NMR (400 MHz, D_2O): δ_H = 2.23 (s, 3H, Me), 7.22 (d, J = 8.1 Hz, 2H, Ar-H), 7.57 (d, J = 7.9 Hz, 2H, Ar-H) ppm. ^{13}C NMR (100 MHz, D_2O) δ = 20.3, 125.2, 129.4, 139.3, 142.5 ppm. Anal. calcd for $C_7H_8O_3S$: C, 48.83; H, 4.68; O, 27.87; S, 18.62%. Found: C, 48.86; H, 4.65%.

4-(Ethoxycarbonyl)benzenesulfonic acid (3d). White crystal, R_f = 0.64 (4 : 1 hexane : EtOAc), yield = 92%; m.p. = 68–70 °C; ^{1}H NMR (400 MHz, D_2O): δ_H = 1.41 (t, J = 7.2 Hz, 3H, Me), 4.42 (q, J = 7.1 Hz, 2H, OCH_2), 7.92 (d, J = 8.3 Hz, 2H, Ar-H), 8.14 (d, J = 8.3 Hz, 2H, Ar-H) ppm. ^{13}C NMR (100 MHz, D_2O) δ = 13.3, 62.5, 125.6, 130.1, 132.3, 146.5, 167.8 ppm. Anal. calcd for $C_9H_{10}O_5S$: C, 46.95; H, 4.38; O, 34.75; S, 13.92%. Found: C, 46.91; H, 4.35%.

4-Fluorobenzenesulfonic acid (3e). White crystal, R_f = 0.66 (4 : 1 hexane : EtOAc), yield = 91%; m.p. = 90–93 °C; ^{1}H NMR (400 MHz, D_2O): δ_H = 7.26–7.35 (m, 2H, Ar-H), 7.84–7.92 (m, 2H, Ar-H) ppm. ^{13}C NMR (100 MHz, D_2O) δ = 115.8, 128.2, 138.5, 164.2 ppm. Anal. calcd for $C_6H_5FO_3S$: C, 40.91; H, 2.86; F, 10.78; O, 27.25; S, 18.20%. Found: C, 40.92; H, 2.84%.

4-Chlorobenzenesulfonic acid (3f). White crystal, R_f = 0.63 (4 : 1 hexane : EtOAc), yield = 95%; m.p. = 94–96 °C; ^{1}H NMR (400 MHz, D_2O): δ_H = 7.32 (d, J = 8.1 Hz, 2H, Ar-H), 7.04 (d, J = 8.3 Hz, 2H, Ar-H) ppm. ^{13}C NMR (100 MHz, D_2O) δ = 126.7, 128.9, 136.6, 140.6 ppm. Anal. calcd for $C_6H_5ClO_3S$: C, 37.41; H, 2.62; Cl, 18.40; O, 24.92; S, 16.64%. Found: C, 37.38; H, 2.65%.

4-Bromobenzenesulfonic acid (3g). White crystal, R_f = 0.61 (4 : 1 hexane : EtOAc), yield = 95%; m.p. = 93–94 °C; ^{1}H NMR (400 MHz, D_2O): δ_H = 7.47–7.52 (m, 2H, Ar-H), 7.51–7.57 (m, 2H, Ar-H) ppm. ^{13}C NMR (100 MHz, D_2O) δ = 125.4, 127.2, 131.8, 141.3 ppm. Anal. calcd for $C_6H_5BrO_3S$: C, 30.40; H, 2.13; Br, 33.71; O, 20.25; S, 13.52%. Found: C, 30.43; H, 2.16%.

2-(Methoxycarbonyl)benzenesulfonic acid (3h). White crystal, R_f = 0.65 (4 : 1 hexane : EtOAc), yield = 92%; m.p. = 64–66 °C; ^{1}H NMR (400 MHz, D_2O): δ_H = 4.02 (s, 3H, OMe), 7.64–7.69 (m, 1H, Ar-H), 7.69–7.76 (m, 2H, Ar-H), 7.99–8.04 (m, 1H, Ar-H) ppm. ^{13}C NMR (100 MHz, D_2O) δ = 53.7, 127.3, 128.2, 130.5, 131.3, 131.7, 139.8, 171.3 ppm. Anal. calcd for $C_8H_8O_5S$: C, 44.44; H, 3.73; O, 37.00; S, 14.83%. Found: C, 44.41; H, 3.76%.

2-Cyanobenzenesulfonic acid (3i). White crystal, R_f = 0.67 (4 : 1 hexane : EtOAc), yield = 91%; m.p. = 120–123 °C; ^{1}H NMR (400 MHz, D_2O): δ_H = 7.62 (t, J = 7.8 Hz, 1H, Ar-H), 7.82–7.87 (m, 1H, Ar-H), 7.99–8.03 (m, 1H, Ar-H), 8.11 (t, J = 1.5 Hz, 1H, Ar-H) ppm. ^{13}C NMR (100 MHz, D_2O) δ = 111.8, 118.7, 129.3, 130.1, 130.3, 135.2, 143.7 ppm. Anal. calcd for $C_7H_5NO_3S$: C, 45.90; H, 2.75; N, 7.65; O, 26.20; S, 17.50%. Found: C, 45.92; H, 2.77%.

[1,1′-Biphenyl]-4-sulfonic acid (3j). White crystal, R_f = 0.65 (4 : 1 hexane : EtOAc), yield = 94%; m.p. = 132–134 °C; ^{1}H NMR (400 MHz, D_2O): δ_H = 7.23–7.31 (m, 3H, Ar-H), 7.41 (d, J = 6.9 Hz, 2H, Ar-H), 7.48 (d, J = 8.3 Hz, 2H, Ar-H), 7.73 (d, J = 8.3 Hz, 2H, Ar-H) ppm. ^{13}C NMR (100 MHz, D_2O) δ = 126.1, 127.1, 127.3, 128.1, 129.1, 139.1, 141.3, 143.2 ppm. Anal. calcd for $C_7H_5NO_3S$: C, 45.90; H, 2.75; N, 7.65; O, 26.20; S, 17.50%. Found: C, 45.92; H, 2.77%.

2-Isopropylbenzenesulfonic acid (3k). White crystal, R_f = 0.62 (4 : 1 hexane : EtOAc), yield = 90%; m.p. = 108–110 °C; ^{1}H NMR (400 MHz, D_2O): δ_H = 1.31 (d, J = 6.9 Hz, 6H, Me), 3.83–3.94 (m,

Published on 22 January 2026. Downloaded by University of California - Los Angeles on 1/28/2026 4:59:03 PM.

1H, CH), 7.33–7.38 (m, 1H, Ar-H), 7.56–7.68 (m, 2H, Ar-H), 7.92 (d, J = 7.9 Hz, 1H, Ar-H) ppm. ^{13}C NMR (100 MHz, D_2O) δ = 23.5, 29.2, 125.9, 126.7, 127.8, 132.2, 139.6, 147.9 ppm. Anal. calcd for $C_7H_5NO_3S$: C, 45.90; H, 2.75; N, 7.65; O, 26.20; S, 17.50%. Found: C, 45.92; H, 2.77%.

4-Sulfobenzoic acid (3l). White crystal, R_f = 0.64 (4 : 1 hexane : EtOAc), yield = 92%; m.p. = 68–71 °C; ^{1}H NMR (400 MHz, D_2O): δ_H = 7.86 (d, J = 8.3 Hz, 2H, Ar-H), 8.04 (d, J = 8.3 Hz, 2H, Ar-H) ppm. ^{13}C NMR (100 MHz, D_2O) δ = 125.7, 130.1, 134.3, 145.8, 170.9 ppm. Anal. calcd for $C_7H_6O_5S$: C, 41.59; H, 2.99; O, 39.57; S, 15.86%. Found: C, 41.56; H, 2.95%.

4-(Methylsulfonyl)benzenesulfonic acid (3m). White crystal, R_f = 0.68 (4 : 1 hexane : EtOAc), yield = 93%; m.p. = 126–127 °C; ^{1}H NMR (400 MHz, D_2O): δ_H = 3.57 (s, 3H, SMe), 7.42 (d, J = 8.3 Hz, 2H, Ar-H), 7.74 (d, J = 8.2 Hz, 2H, Ar-H) ppm. ^{13}C NMR (100 MHz, D_2O) δ = 22.3, 125.9, 126.1, 138.8, 142.7 ppm. Anal. calcd for $C_7H_8O_5S_2$: C, 35.59; H, 3.41; O, 33.86; S, 27.14%. Found: C, 35.54; H, 3.45%.

3,5-Dimethylbenzenesulfonic acid (3n). White crystal, R_f = 0.71 (4 : 1 hexane : EtOAc), yield = 91%; m.p. = 122–125 °C; ^{1}H NMR (400 MHz, D_2O): δ_H = 2.33 (s, 6H, Me), 7.24 (s,1H, Ar-H), 7.41 (s, 2H, Ar-H) ppm. ^{13}C NMR (100 MHz, D_2O) δ = 20.4, 122.6, 132.9, 139.5, 142.3 ppm. Anal. calcd for $C_8H_{10}O_3S$: C, 51.60; H, 5.41; O, 25.77; S, 17.22%. Found: C, 51.56; H, 5.46%.

3-Phenylpropane-1-sulfonic acid (3o). White crystal, R_f = 0.69 (4 : 1 hexane : EtOAc), yield = 92%; m.p. = 101–105 °C; ^{1}H NMR (400 MHz, D_2O): δ_H = 1.91–2.04 (m, 2H, CH_2), 2.68 (m, 2H, CH_2), 2.86 (m, 2H, CH_2), 7.19–7.25 (m, 3H, Ar-H), 7.27 (t, J = 7.3 Hz, 2H, Ar-H) ppm. ^{13}C NMR (100 MHz, D_2O) δ = 25.6, 33.4, 50.5, 126.3, 128.6, 128.5, 141.6 ppm. Anal. calcd for $C_9H_{12}O_3S$: C, 53.98; H, 6.04; O, 23.97; S, 16.01%. Found: C, 53.92; H, 6.09%.

5-Phenylpentane-1-sulfonic acid (3p). White crystal, R_f = 0.67 (4 : 1 hexane : EtOAc), yield = 94%; m.p. = 99–102 °C; ^{1}H NMR (400 MHz, D_2O): δ_H = 1.18–1.27 (m, 2H, CH_2), 1.38–1.51 (m, 2H, CH_2), 1.59–1.71 (m, 2H, CH_2), 2.43 (t, J = 7.2 Hz, 2H, CH_2), 2.71–2.79 (m, 2H, CH_2), 7.03–7.08 (m, 3H, Ar-H), 7.14 (t, J = 7.2 Hz, 2H, Ar-H) ppm. ^{13}C NMR (100 MHz, D_2O) δ = 24.1, 27.7, 30.4, 35.2, 51.3, 125.5, 128.4, 128.5, 142.6 ppm. Anal. calcd for $C_{11}H_{16}O_3S$: C, 57.87; H, 7.06; O, 21.02; S, 14.04%. Found: C, 57.83; H, 7.11%.

Result and discussion

The synthesized catalyst was comprehensively characterized using multiple analytical techniques to clarify its structure, composition, and function. FT-IR identified surface functional groups, while XRD determined crystalline phases and structural ordering. SEM provided microstructural and particle size information, and EDS/EDX mapping established elemental composition and spatial distribution. BET analysis quantified specific surface area and porosity, and TGA assessed thermal stability and decomposition behavior. XPS probed elemental oxidation states and bonding environments, whereas cyclic voltammetry evaluated the catalyst's electrochemical behavior and potential reaction mechanisms under operating conditions.

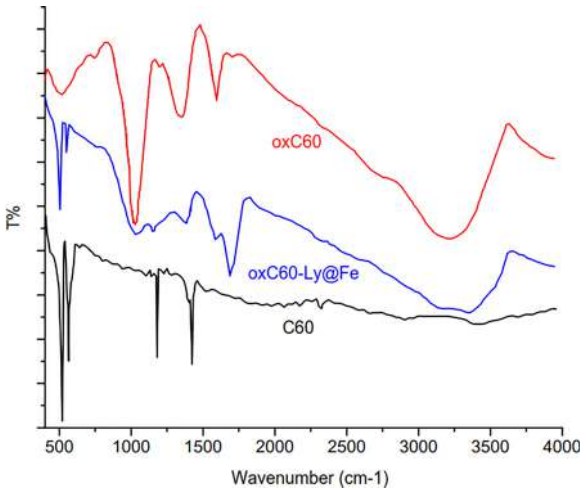


Fig. 8 FT-IR analysis of C_{60}, oxC_{60}, and oxC_{60}–Ly@Fe.

The results of the FT-IR analysis are shown in Fig. 8. According to these results, the black curve corresponds to C_{60}. The FT-IR spectrum of pristine C_{60} fullerene exhibits a limited number of characteristic absorption peaks due to its highly symmetric icosahedral structure, which restricts the number of IR-active vibrational modes. The most prominent bands appear at approximately 527, 571, 1186, and 1430 cm^{-1}, each corresponding to specific vibrational transitions within the fullerene cage. The band at around 527 cm^{-1} is attributed to tangential deformation modes of the carbon framework, representing the bending vibrations of the fused pentagonal and hexagonal rings. The peak at 571 cm^{-1} corresponds to a radial breathing-type vibration associated with symmetric stretching of C–C bonds directed toward and away from the molecular center, reflecting the spherical integrity of the C_{60} cage. The absorption near 1186 cm^{-1} is assigned to tangential C–C stretching vibrations along the fullerene surface, indicative of conjugated sp^2 carbon bonding. The most intense peak at 1430 cm^{-1} arises from in-plane stretching of C=C double bonds, confirming the presence of delocalized π-electron systems within the carbon network. The absence of any additional peaks, such as those associated with oxygen-containing functional groups (*e.g.*, O–H around 3400 cm^{-1} or C=O near 1700 cm^{-1}), indicates that the material is chemically pure and structurally intact, with no surface oxidation or functionalization. This spectral profile is therefore characteristic of high-purity pristine fullerene C_{60}.

The FT-IR spectrum of oxidized fullerene (oxC_{60}, red curve) exhibits significant differences compared to pristine C_{60}, confirming the successful introduction of oxygen-containing functional groups. New absorption bands appear at 548 cm^{-1}, which are attributed to wagging vibrations of hydroxyl (–OH) groups. Furthermore, prominent bands arise between 1043 and 1399 cm^{-1}, including a peak at 1043 cm^{-1} assigned to the C–O–C ether (epoxide) stretch, and peaks at 1399 cm^{-1} corresponding to C–OH stretching vibrations. An intense band observed near 1624 cm^{-1} and 3262 cm^{-1} is generally associated with bending modes of C=O and CO_2H functional group. These spectral features collectively confirm the successful covalent functionalization of the C_{60} cage with oxygen-bearing groups such as epoxides, hydroxyls,

 This journal is © The Royal Society of Chemistry and the Centre National de la Recherche Scientifique 2026

Published on 22 January 2026. Downloaded by University of California - Los Angeles on 1/28/2026 4:59:03 PM.

and possibly carbonyl moieties formed during the oxidation process. The presence of these functional groups alters the electronic and chemical properties of fullerene, enhancing solubility and reactivity, which is advantageous for subsequent applications.

The FT-IR spectrum of the synthesized catalyst oxC$_{60}$–Ly@Fe (blue curve) displays distinctive absorption bands that substantiate the successful functionalization of fullerene oxide with L-lysine and the coordination of Fe species. The bands at 531 and 576 cm^{-1} are indicative of vibrations associated with the C$_{60}$ fullerene cage and Fe–O bonds, confirming the retention of the fullerene backbone and the presence of iron–oxygen functional groups. The absorption peak at 1084 cm^{-1} corresponds to C–O stretching vibrations, which are typical of ether or epoxide groups introduced during oxidation and further functionalization. The bands at 1187 and 1413 cm^{-1} are attributed to C–N and C–H bending vibrations, supporting the covalent attachment of the L-lysine moiety to the oxidized fullerene surface. Furthermore, the broad absorptions observed at 3159 and 3385 cm^{-1} correspond to O–H and N–H stretching vibrations, respectively, indicating the presence of hydroxyl and carboxylic acid groups, alongside amino functionalities originating from L-lysine. The peak at 1632 cm^{-1} is characteristic of C=O stretching vibrations from amide or carboxyl groups, confirming effective grafting of the amino acid ligand. Additionally, the band appearing at 1715 cm^{-1} signifies carbonyl groups linked to the coordination of Fe species. Collectively, these spectral features affirm the successful covalent modification of oxidized fullerene with L-lysine and the incorporation of Fe, resulting in a catalyst with a unique chemical environment and improved functional properties.

XRD analysis of the C$_{60}$ sample (Fig. 9, black curve) confirms a well-defined crystalline structure characteristic of pristine fullerene. The diffraction pattern exhibits prominent peaks at 2θ values of approximately 9.06°, 16.2°, and 19.4°, which correspond to the (111), (222), and (311) crystallographic planes of the face-centered cubic (fcc) lattice, respectively. These distinct peaks affirm the high crystallinity and ordered cubic packing of C$_{60}$ molecules in the solid state. The sharpness and intensity of these peaks indicate the preservation of the spherical shape and icosahedral symmetry of the fullerene cage, which is vital for maintaining its unique electronic and mechanical properties. The regular repetition of these lattice planes contributes to the molecular stability and characteristic behavior of fullerene materials. In contrast, the XRD pattern of the oxC$_{60}$ (Fig. 9, red curve) exhibits diffraction peaks at 2θ values of 31.3°, 32.7°, 33.0°, 35.9°, 37.2°, and 44.6°, marking significant lattice modifications due to oxidation. The peak observed at 31.3° reflects lattice expansion caused by oxygen-containing functional groups such as epoxides, hydroxyls, or carbonyls intercalated within the fullerene matrix. Peaks at 32.7° and 33.0° suggest structural rearrangements and possible formation of new oxidized phases. Peaks at 35.9°, 37.2°, and 44.6° indicate distortions in lattice parameters due to altered carbon frameworks or domains with varying packing densities, highlighting successful covalent functionalization that modifies the crystal environment and impacts electronic and chemical properties, essential for catalysis and material applications.

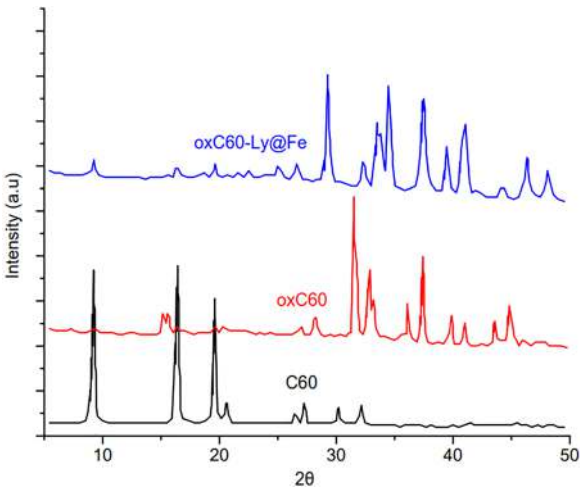


Fig. 9 XRD analysis of C$_{60}$, oxC$_{60}$, and oxC$_{60}$–Ly@Fe.

The XRD analysis of the oxC$_{60}$–Ly@Fe catalyst (Fig. 9, blue curve) shows an even more complex diffraction pattern with peaks at 29.1°, 33.4°, 34.6°, 35.9°, 37.3°, 39.4°, 40.9°, 46.2°, and 48.1°, reflecting the multifaceted crystalline structure induced by L-lysine functionalization and Fe incorporation. The 29.1° peak corresponds to fullerene lattice planes slightly distorted by metal coordination, while peaks at 33.4° and 34.6° signify lattice strain or new phases due to Fe coordination. Peaks at 35.9° and 37.3° correspond to Fe–O or related species, evidencing Fe integration into the matrix. The 39.4° and 40.9° peaks likely arise from overlapping fullerene and iron-containing crystalline domains, indicating synergistic interaction. The high-angle reflections at 46.2° and 48.1° indicate the presence of well-ordered crystalline domains. Together, these XRD patterns illustrate how L-lysine grafting and Fe modification transform the crystalline structure, producing a multi-phase catalyst combining original fullerene crystallinity with new iron-related phases. This multi-phase crystallinity enhances the catalyst's chemical activity and stability, as modifications create active sites and improve electron transfer within the catalytic framework.

Fig. 10 presents the scanning electron microscopy (SEM) images of C$_{60}$ (panels a and b) and oxC$_{60}$–Ly@Fe (panels c and d) samples at different magnifications, demonstrating distinct morphological features due to functionalization and metal modification. Panels a and b illustrate the C$_{60}$ sample, revealing a uniform dispersion of spherical particles with smooth surfaces. The particles are well-defined with narrow size distribution, predominantly ranging from sub-micron to a few micrometers, forming a densely packed morphology. The high degree of regularity and absence of surface roughness reflect the pristine nature of C$_{60}$, consistent with its crystalline and molecularly symmetric structure.

In contrast, panels c and d illustrate the surface morphology of the oxC$_{60}$–Ly@Fe catalyst. The images demonstrate significant changes in particle texture and aggregation compared to pristine C$_{60}$. The particles appear larger and more irregular with rough, porous surfaces, indicative of successful oxidation

Published on 22 January 2026. Downloaded by University of California - Los Angeles on 1/28/2026 4:59:03 PM.

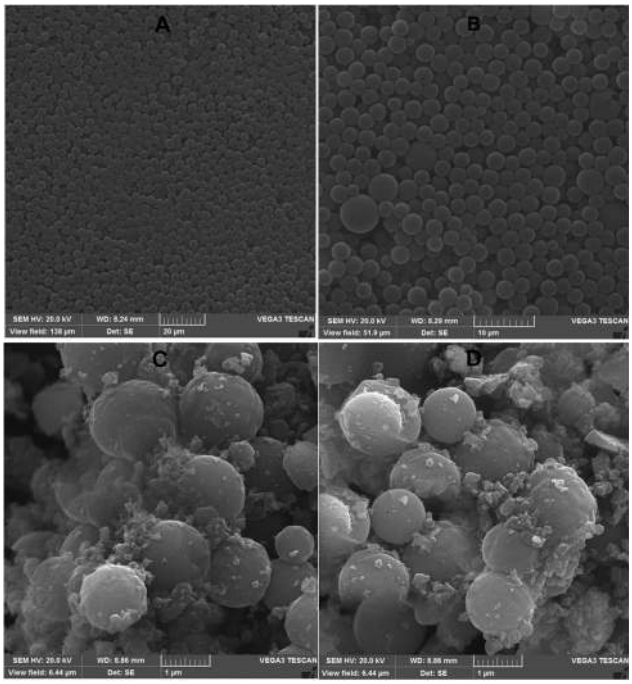


Fig. 10 SEM analysis of (a) and (b) C_{60} and (c) and (d) oxC_{60}–Ly@Fe.

and functionalization with L-lysine and Fe incorporation. The aggregation of spherical particles into Grape-like agglomerated microsphere clusters suggests strong inter-particle interactions likely mediated by the organic ligand and metal sites. The roughened surface textures and irregular particle sizes confirm the introduction of defects and a more complex surface chemistry, which are beneficial for increasing the catalyst's surface area and active sites for enhanced catalytic performance. Overall, the SEM analysis highlights the morphological transformation from smooth, uniform fullerene spheres to rough, aggregated, and functionalized clusters in oxC_{60}–Ly@Fe, demonstrating effective chemical modification that impacts surface chemistry and catalytic behavior.

The EDS spectra presented in Fig. 11 confirm the elemental composition of the synthesized materials at different stages of modification. Spectrum A, corresponding to pristine C_{60}, shows a dominant peak associated solely with carbon, confirming the high purity of the fullerene and the absence of heteroatom contamination. In spectrum B, attributed to oxC_{60}, in addition to the carbon peak, a distinct oxygen signal is observed, which verifies the successful oxidation of the fullerene cage and the introduction of oxygen-containing functional groups, such as C–O, C═O, and O–C═O. The relative increase in oxygen content compared to pristine C_{60} indicates enhanced surface functionalization, which improves the reactivity and dispersibility of oxC_{60} in polar media.

Spectrum C, corresponding to oxC_{60}–Ly@Fe, displays carbon and oxygen peaks along with noticeable nitrogen and Fe signals. The appearance of nitrogen confirms the successful incorporation of L-lysine (Ly), which contains amine and carboxyl functional groups. Furthermore, the Fe peaks provide clear evidence of Fe immobilization onto the oxC_{60}–Ly support, indicating successful metal loading. The coexistence of carbon, oxygen, nitrogen, and Fe elements in the final composite verifies the stepwise functionalization and formation of the Fe-supported fullerene-based nano catalyst.

The EDX elemental mapping analysis of the oxC_{60}–Ly@Fe nanocomposite confirms the uniform spatial distribution of all

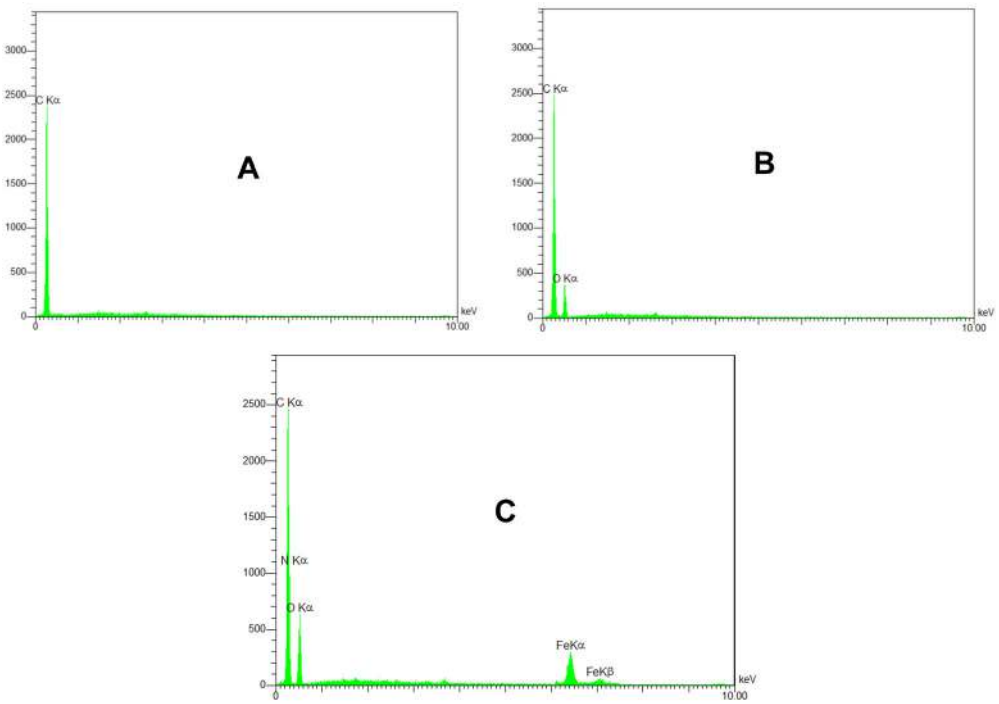


Fig. 11 EDS analysis of (a) C_{60}, (b) oxC_{60}, and (c) oxC_{60}–Ly@Fe.

 This journal is © The Royal Society of Chemistry and the Centre National de la Recherche Scientifique 2026

Published on 22 January 2026. Downloaded by University of California - Los Angeles on 1/28/2026 4:59:03 PM.

constituent elements across the sample surface. The carbon map illustrates the dominant presence of carbon originating from the C_{60} backbone, providing evidence of a continuous carbonaceous structure. The oxygen signal is homogeneously dispersed, indicating successful oxidation of the fullerene surface and the formation of oxygen-containing functional groups, which play a crucial role in anchoring other components. The nitrogen distribution further verifies the incorporation of L-lysine onto the oxC_{60} surface, demonstrating effective functionalization through nitrogen-containing moieties from the amino acid structure. Additionally, the Fe map shows a well-dispersed distribution of Fe NPs throughout the composite, confirming their successful immobilization and preventing aggregation. The uniform co-localization of carbon, oxygen, nitrogen, and Fe elements supports the successful stepwise synthesis of the oxC_{60}–Ly@Fe hybrid structure and suggests strong interactions among the components (Fig. 12).

Fig. 13 illustrates the nitrogen adsorption–desorption isotherms for pristine C_{60}, oxC_{60}, and the functionalized catalyst oxC_{60}–Ly@Fe. For the C_{60} sample, the isotherm resembles a Type II isotherm, characteristic of mesoporous materials with unrestricted monolayer-multilayer adsorption. The initial sharp uptake at low relative pressure ($P/P_0 < 0.1$) indicates strong adsorbate–surface interactions, followed by a gradual increase as multilayer adsorption proceeds. The minimal hysteresis loop suggests a surface with limited mesoporosity and primarily external surface adsorption. The oxC_{60} isotherm demonstrates a noticeable change with enhanced adsorption capacity and a more pronounced hysteresis loop appearing in the relative pressure range 0.4 to 0.8, indicative of mesoporous structure development due to oxidation and introduction of oxygen-containing functional groups. This change signifies a decrease in surface area and increases pore volume and average pore compared to pristine C_{60}. The hysteresis loop indicates capillary condensation in mesopores, reflecting pore size distribution heterogeneity introduced upon oxidation. The oxC_{60}–Ly@Fe sample exhibits further enhanced adsorption behavior with a more significant hysteresis loop similar in shape to oxC_{60} but with lower volume adsorbed across the pressure range, indicating increased mesoporosity and surface area resulting from L-lysine functionalization and Fe incorporation.

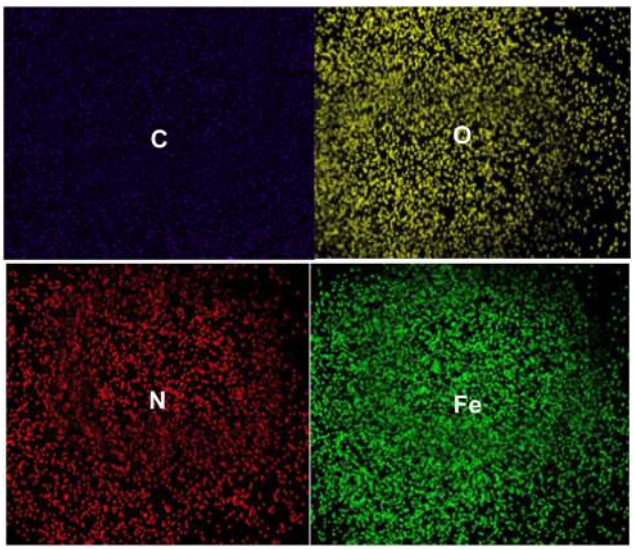


Fig. 12 EDX mapping analysis of oxC_{60}–Ly@Fe.

The BET analysis summarized in Table 2 provides important insights into the textural properties of C_{60}, oxC_{60}, and oxC_{60}–Ly@Fe. The pristine C_{60} exhibits a relatively high specific surface area of 404 $m^2\ g^{-1}$, a pore volume of 0.17 $cm^3\ g^{-1}$, and an average pore diameter of 1.7 nm, which lies at the boundary between micro- and mesoporous structures. After oxidation, the surface area slightly decreases to 384.9 $m^2\ g^{-1}$ for oxC_{60}, while the pore volume increases significantly to 0.36 $cm^3\ g^{-1}$, and the average pore size expands to 3.7 nm, indicating the introduction of oxygen-containing functional groups. These groups likely disrupt the fullerene packing and open new mesoporous channels, enhancing the porosity. Upon further functionalization with L-lysine and incorporation of Fe NPs to form oxC_{60}–Ly@Fe, the surface area decreases further to 351.7 $m^2\ g^{-1}$ due to partial blockage of pores by the organic ligand and metal species. Similarly, the pore volume slightly reduces to 0.29 $cm^3\ g^{-1}$, while the average pore diameter remains within the mesoporous range at 3.4 nm. Despite the decrease in surface area, the preserved mesoporous structure facilitates mass transfer and provides accessible active sites, confirming that oxC_{60}–Ly@Fe retains suitable textural properties for catalytic applications.

TGA curve of the C_{60} sample shows a distinct thermal degradation behavior with a significant mass loss event occurring at approximately 390 °C. The sample remains thermally stable up to this temperature, indicating that the pristine fullerene structure maintains its integrity under heating. At around 390 °C, a sharp and substantial mass loss of 99.2% is observed, corresponding to the decomposition or sublimation of the fullerene material. This dramatic weight loss signifies the transition from the solid fullerene phase to gaseous degradation products, consistent with the known thermal properties of C_{60}, which sublimes or decomposes at high temperatures. The steep slope in the derivative thermogravimetric (DTG) curve corroborates the rapid degradation process within a narrow temperature range, illustrating the high purity and uniformity of the sample with a single major degradation step (Fig. 14a). The TGA and DTG curves of oxC_{60} reveal a complex multi-step thermal decomposition process. Around 322 °C, a sharp DTG peak corresponds to nearly 19% mass loss, likely from the breakdown of stable carbonyl or carboxyl groups (Fig. 14b). A much larger and steeper mass loss, approximately 56%, occurs at about 380 °C, indicating the catastrophic collapse of the fullerene cage, rapid volatilization, and gas release. After 400 °C, the residual mass stabilizes with minimal further change, suggesting the formation of thermally robust graphitic or partially oxidized carbon material. These results demonstrate that oxC_{60} decomposes through several well-defined thermal events, and its oxygen-containing defects promote stepwise degradation, resulting in greater thermal stability and residue compared to pristine C_{60}. The TGA spectrum of oxC_{60}–Ly@Fe, an oxidized C_{60} fullerene functionalized with L-

Published on 22 January 2026. Downloaded by University of California - Los Angeles on 1/28/2026 4:59:03 PM.

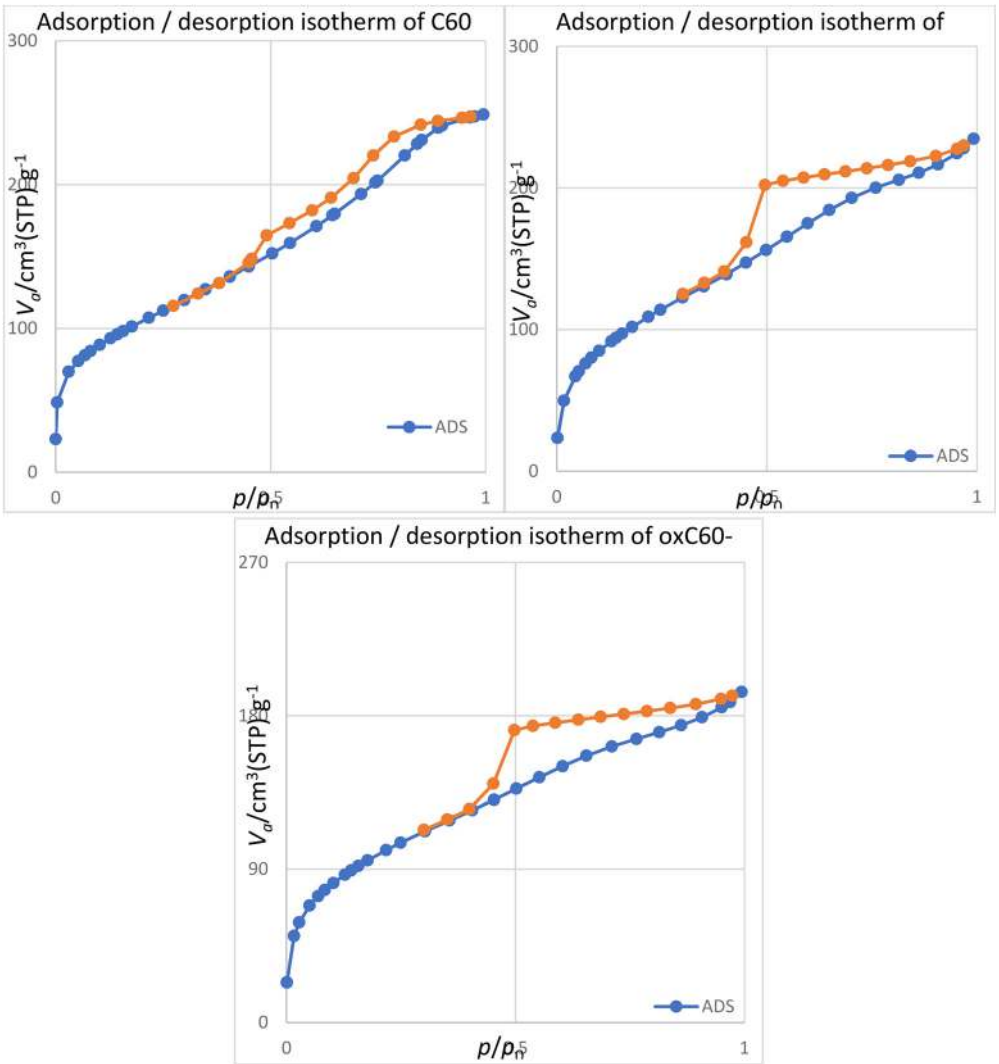


Fig. 13 BET of C_{60}, oxC_{60} and oxC_{60}–Ly@Fe.

Table 2 BET analysis of C_{60}, oxC_{60} and oxC_{60}–Ly@Fe

Sample	BET surface area [m^2 g^{-1}]	Pore volume [cm^3 g^{-1}]	Average pore diameter [nm]	Type of pore
C_{60}	404	0.17	1.7	Mesoporous
oxC_{60}	384.9	0.36	3.7	Mesoporous
oxC_{60}–Ly@Fe	351.7	0.29	3.4	Mesoporous

lysine and loaded with Fe, reveals a multi-stage thermal degradation profile reflecting its composite nature (Fig. 14c). Initial mass loss of 4.93% at 110 °C is due to the evaporation of moisture and solvents, followed by a 12.82% loss at 220 °C from L-lysine breakdown and weaker C–O bond cleavage. A gradual decline to 19.77% by 460 °C suggests the loss of resilient oxygen groups, while a sharp 46.66% loss at 540 °C indicates major fullerene cage rupture, possibly catalyzed by Fe. The process concludes with a total loss of 84.16% by 700–800 °C, leaving a 15.84% residue of Fe–O or metal–carbon composites. To a dust indicating 15% Cu metal coated on the catalyst.

The high-resolution XPS analysis of oxC_{60}–Ly@Fe is illustrated in Fig. 15. The survey spectrum (Fig. 15A) confirms the presence of characteristic peaks for C 1s, N 1s, O 1s, and Fe 2p, identifying the principal elemental composition of the material. The C 1s spectrum (Fig. 15B) is deconvoluted into five distinct peaks, corresponding to C–C (291.2 eV), C═C (290 eV), C–O (288.7 eV), C═O (287 eV), and C–N (285 eV) bonds, indicative of diverse carbon bonding environments. The O 1s spectrum (Fig. 15C) exhibits peaks at binding energies of 528.8 eV, 527.8 eV, and 525.9 eV, which are attributable to C–O, C═O, and Fe–O bonds, respectively, consistent with the presence of carbonyl, ether/hydroxyl, and amide functionalities. The N 1s spectrum (Fig. 15D) displays peaks at 392.4 eV and 391.9 eV, assigned to C–N and Fe–N bonds, respectively. The Fe 2p high-resolution spectrum (Fig. 15E) reveals characteristic peaks at 723 eV and 710.5 eV, ascribed to Fe(II), reveals characteristic peaks at 725.2 and 711.8 eV and 710.5 eV, ascribed to Fe(III) oxidation states, respectively, suggesting that the predominant form of Fe in oxC_{60}–Ly@Fe is oxidized, with a minor contribution from metallic Fe. These findings collectively elucidate the complex chemical

 This journal is © The Royal Society of Chemistry and the Centre National de la Recherche Scientifique 2026

Published on 22 January 2026. Downloaded by University of California - Los Angeles on 1/28/2026 4:59:03 PM.

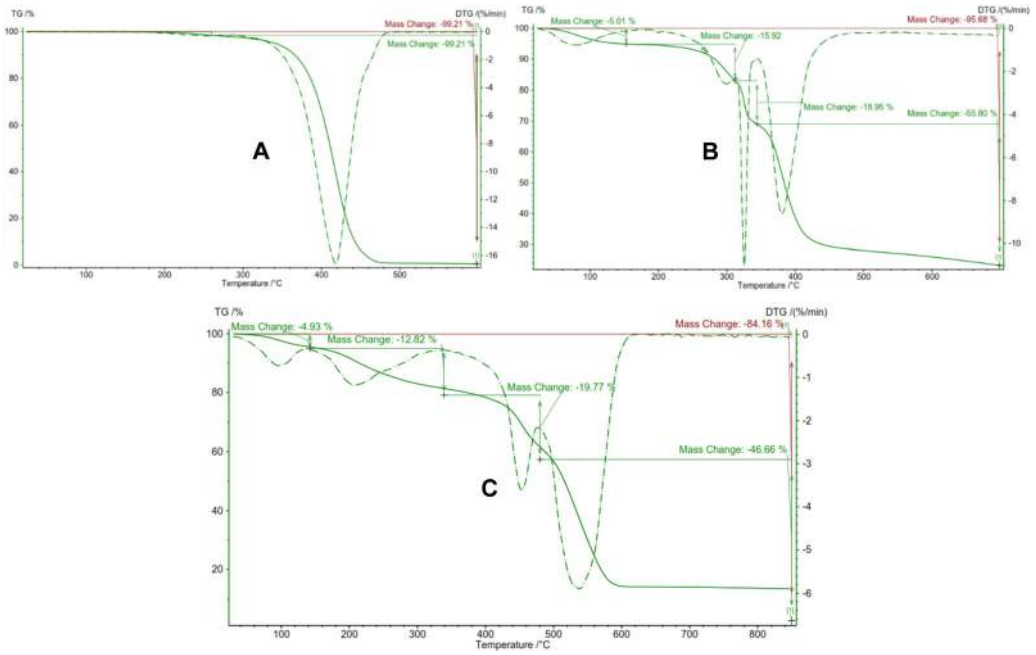


Fig. 14 TGA analysis of (a) C_{60}, (b) oxC_{60}, and (c) oxC_{60}–Ly@Fe.

environment and oxidation states of the constituent elements within the synthesized material.

Fig. 16 presents the cyclic voltammetry (CV) analysis results, investigating the influences of current, electrolyte type, and electrode material on the electrosynthesis process. In Fig. 16A, CV curves obtained at currents of 5, 10, 15, and 20 mA show that the potential window peaks at 10 mA, while 15 mA is identified as the optimal current for the highest reaction efficiency. Fig. 16B compares various electrolytes including NaCl, NaBr, and urea/choline chloride (urea/ChCl) DES. Among these, urea/ChCl DES demonstrates superior performance due to its ability to form extensive hydrogen bonding networks and provide an ionic environment, which enhances electrical conductivity, stabilizes reaction intermediates, and lowers activation energy barriers, thereby improving electrocatalytic efficiency. The effect of electrode type is examined through CV measurements using Fe rod, Fe foam, and the synthesized oxC_{60}–Ly@Fe GCE electrodes. Notably, the oxC_{60}–Ly@Fe GCE electrode exhibits a wider potential window and more efficient electron transfer kinetics, resulting in greater catalytic activity compared to Fe rod and Fe foam electrodes. These electrochemical findings are consistent with the optimization data presented in the accompanying table, validating the superior catalytic performance of the oxC_{60}–Ly@Fe GCE electrode in the studied electrosynthesis.

The optimization of the electrocatalytic reaction between chlorobenzene **1(a)** and S_8 **2(a)** was systematically performed in a 50 mL electrolysis cell equipped with a graphite rod anode, Fe rod cathode, heater-stirrer, and a 1 cm magnetic stir bar. MeOH served as the initial solvent, and NaCl (30%) as the electrolyte under ambient temperature for 4 hours at an applied current of 25 mA, resulting in a modest 24% yield (Table 3, entry 1). Exploration of alternative solvents EtOH, iPrOH, DMF, H_2O, and MeCN produced improved yields of 29%, 31%, 35%, 28%, and 42%, respectively (Table 3, entries 2–6). Switching the electrolyte from NaCl to NaBr raised the yield to 48%, while an increased concentration of NaBr (50%) had no additional effect (Table 3, entries 7 and 8). Temperature elevation to 70 °C led to a yield of 49%, signifying negligible improvement with conventional parameter changes (Table 3, entry 9). Remarkable improvement was achieved by employing ChCl/urea DES as both solvent and electrolyte, increasing yield to 60% (Table 3, entry 10), attributed to the DES high ionic conductivity, enhanced intermediate stabilization, and a reduction in reaction energy barrier. Evaluation of different cathodes Fe foam, Pt rod, and oxC_{60}–Ly@Fe GCE increased yields to 74%, 91%, and 94%, respectively, with oxC_{60}–Ly@Fe GCE outperforming even Pt, thus significantly increasing the system commercial viability (Table 3, entries 11–13).

Optimization of the applied current indicated no further increase in yield when decreasing from 25 to 20 or 15 mA; the yield remained at 94% (Table 3, entries 14–15). However, a decrease to 10 mA resulted in a reduced yield of 79% (Table 3, entry 16), establishing 15 mA as optimal. Similarly, reducing reaction time from 4 to 3 and 1 hour maintained a 94% yield, whereas 0.5 hour resulted in only 61% (Table 3, entries 17–19), indicating 1 hour as the optimal reaction duration. Consequently, the optimal conditions established were 15 mA current, 1 hour reaction time, ambient temperature, and an oxC_{60}–Ly@Fe GCE anode. Mechanistic investigations showed that no product was formed in the absence of oxygen, confirming the requirement of O_2 for S_8 oxidation to SO_3H (Table 3, entry 20). Additionally, graphite rod electrodes under atmospheric O_2 also failed to yield product, establishing the pivotal role of Fe

Published on 22 January 2026. Downloaded by University of California - Los Angeles on 1/28/2026 4:59:03 PM.

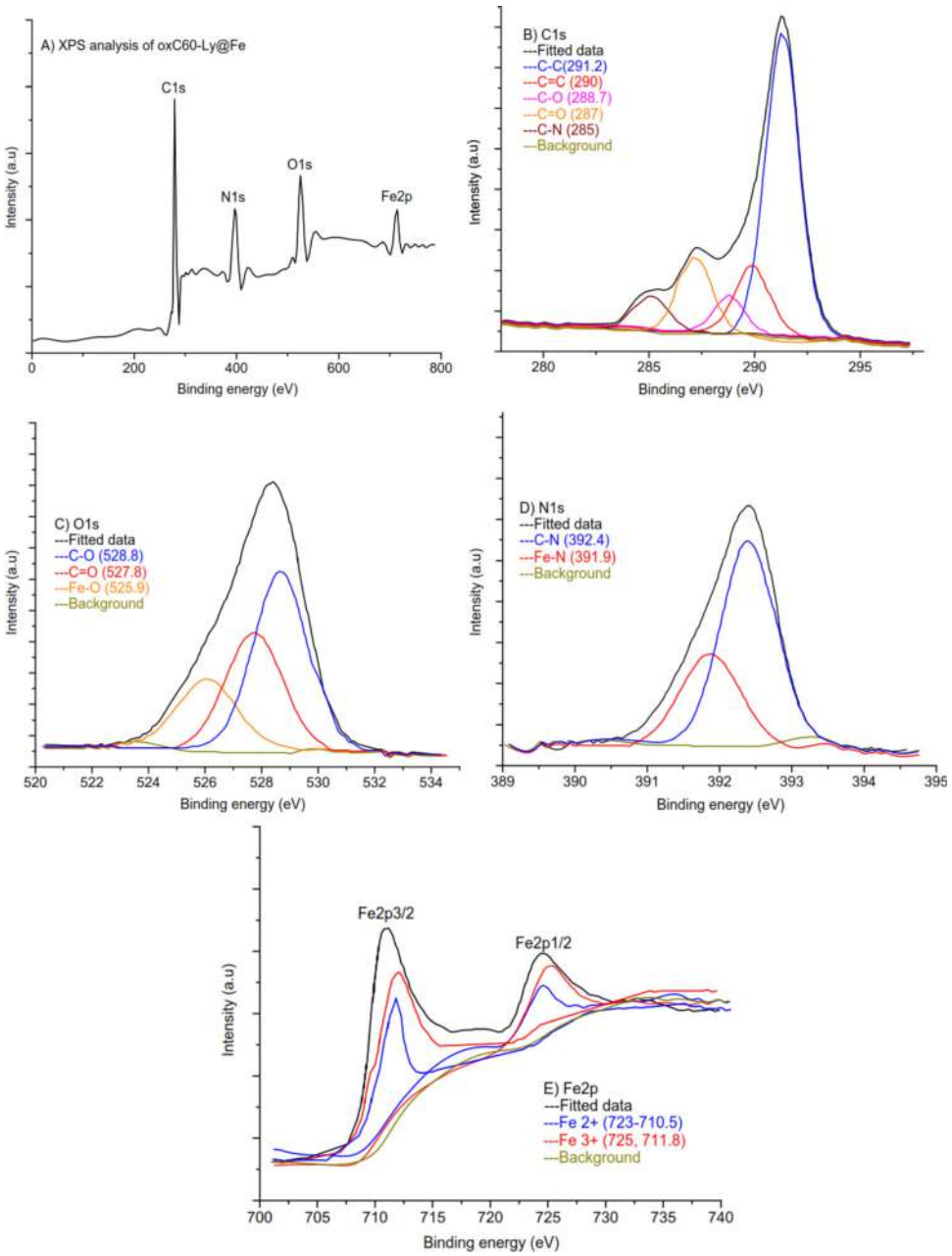


Fig. 15 XPS analysis of oxC_{60}–Ly@Fe.

in facilitating the oxidation (Table 3, entry 21). Strikingly, the reaction conducted under nitrogen with the addition of 0.5 mL distilled H_2O (3 eq.) achieved a 91% yield (Table 3, entry 22), demonstrating that in the presence of H_2O, the process proceeds efficiently even without atmospheric O_2, further highlighting the efficacy of the optimized electro-catalytic conditions.

After optimization of the reaction conditions, a series of benzenesulfonic acid derivatives **3(a–p)** were synthesized using chlorobenzene **2(a–p)** and S_8 **2(a)** as reagents, yielding products with excellent isolated yields ranging from 90% to 97%. The catalytic system employed demonstrated robust activity throughout the process. To evaluate the environmental impact of the synthesis, the E factor was determined, revealing low values between 0.03 and 0.11, indicative of a process with minimal waste generation and high environmental compatibility. Further assessment of the chemical efficiency was conducted *via* calculation of the atom economy for the synthesized derivatives, which ranged from 82% to 87%, underscoring the process's high synthetic efficiency. Additionally, the catalytic performance was quantitatively analyzed by turnover number (TON) and turnover frequency (TOF), which were found to vary from 141 to 211 and 2.75 to 3.5, respectively. These metrics reflect the high catalytic activity and stability of the electrocatalytic system employed in this study.

TON and TOF measurements highlight the efficiency of the catalytic system, providing insight into its potential for scale-up and commercial applications. Overall, this electrochemical

 This journal is © The Royal Society of Chemistry and the Centre National de la Recherche Scientifique 2026

Published on 22 January 2026. Downloaded by University of California - Los Angeles on 1/28/2026 4:59:03 PM.

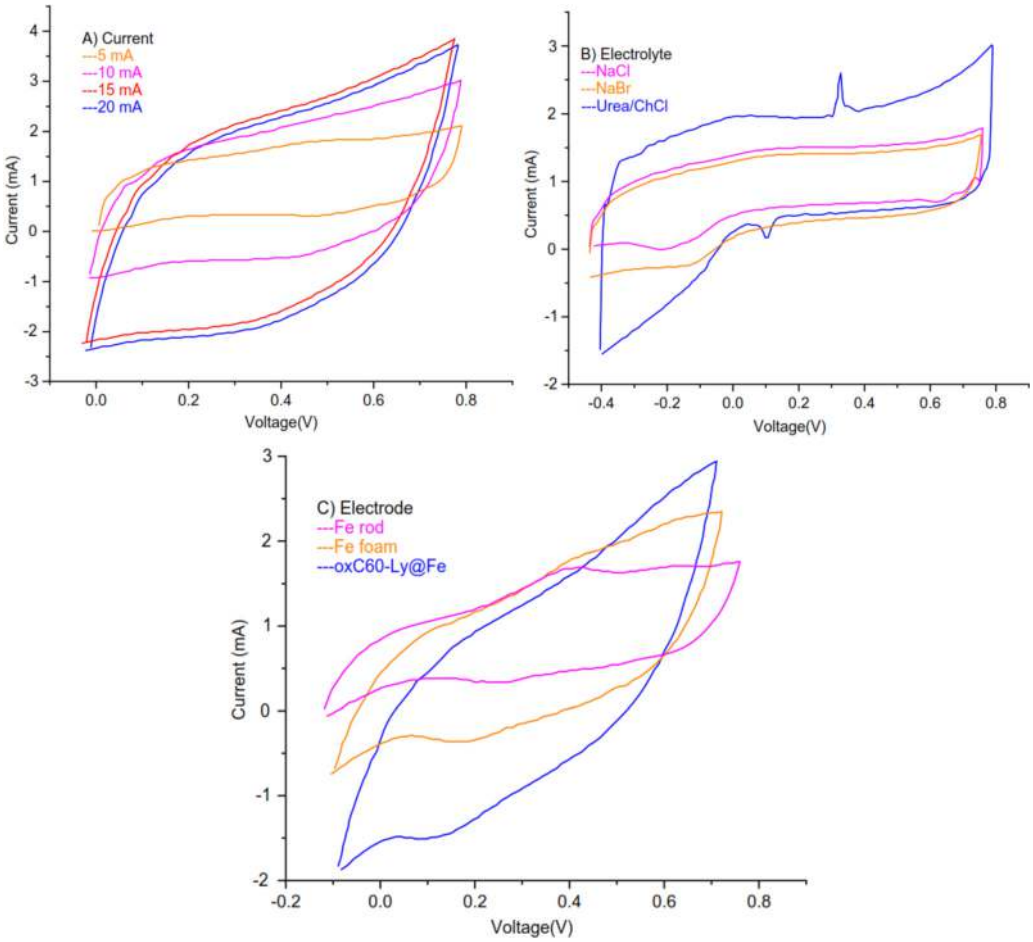


Fig. 16 Evaluation of different types of (a) currents, (b) electrolytes, and (c) electrodes.

protocol aligns with green chemistry principles by minimizing environmental impact, maximizing material utilization, and enabling economically attractive and scalable synthesis of sulfonic acid derivatives.

The reaction mechanism illustrated in Fig. 17 proceeds through a well-defined sequence of electrochemical activation and organometallic transformations. In the first step, chloride ions (Cl^-) present in the electrolyte are oxidized at the anode to generate molecular chlorine (Cl_2), which serves as a reactive halogenating agent.[44] The *in situ* generated chlorine reacts with Fe to produce $FeCl_2$ and $FeCl_3$ *via* a redox process. This $FeCl_2$ and $FeCl_3$ species subsequently coordinates with chlorobenzene **1(a)**, forming the transient organometallic intermediate phenyliron(III) chloride **(a)**. This intermediate constitutes the catalytic core of the reaction and initiates the iron-mediated transformation pathway (represented as the green catalytic cycle in the figure). Simultaneously, S_8 **2(a)** undergoes electrophilic activation by chlorine, resulting in ring cleavage and the formation of eight moles of sulfur dichloride (SCl_2) **(b)**. The lone pair on the sulfur atom in SCl_2 acts as a nucleophile and attacks the phenyliron(III) chloride intermediate **(a)**. This nucleophilic substitution displaces $FeCl_2$ and $FeCl_3$ and generates a key sulfur-containing intermediate, trichloro(phenyl)-λ^4-sulfane **(c)**, which represents a crucial branching point in the reaction pathway.

From this stage, the mechanism diverges into two possible oxidative routes. In the presence of atmospheric O_2, molecular O_2 participates directly in the oxidation of the sulfane intermediate. Alternatively, in an oxygen-free environment (N_2 atmosphere), the reaction can still proceed through hydrolytic oxidation in the presence of three equivalents of water, demonstrating that the system is not strictly dependent on external oxygen. In both scenarios, a nucleophilic attack by oxygen occurs on the sulfane intermediate, leading to stepwise dechlorination and oxidative transformation. Initially in the proposed radical electrochemical pathway, H_2O or dissolved oxygen undergoes anodic oxidation at the electrode surface, leading to the formation of oxygen radical anions and/or hydroxyl radicals. Then, chlorination of sulfur generates S–Cl functionalities that strongly withdraw electron density from the sulfur center, rendering it the most electrophilic and thus the weakest site in the intermediate. Under these conditions, oxygen-centered radicals or nucleophiles ($^{\bullet}OH$, $RO^{\bullet}$, or H_2O/O_2-derived species) preferentially attack sulfur rather than chlorine, populating the antibonding σ^* orbital of the S–Cl bond, which is primarily localized on sulfur. This interaction

Published on 22 January 2026. Downloaded by University of California - Los Angeles on 1/28/2026 4:59:03 PM.

Table 3 Optimization electro-catalytic reaction conditions for synthesis of Benzenesulfonic acids **3(a–p)**



Entry	X^b (eq.)	Current (mA)	Time (h)	Heat (°C)	Solvent	Yield[a] (%)
1	NaCl[c]	25	4	r.t.	MeOH	24[ei]
2	NaCl[c]	25	4	r.t.	EtOH	29[ei]
3	NaCl[c]	25	4	r.t.	iPrOH	31[ei]
4	NaCl[c]	25	4	r.t.	DMF	35[ei]
5	NaCl[c]	25	4	r.t.	H_2O	28[ei]
6	NaCl[c]	25	4	r.t.	MeCN	42[ei]
7	NaBr[c]	25	4	r.t.	MeCN	48[ei]
8	NaBr[d]	25	4	r.t.	MeCN	48[ei]
9	NaBr[c]	25	4	70	MeCN	49[ei]
10	Urea/ChCl	25	4	r.t.	—	60[ei]
11	Urea/ChCl	25	4	r.t.	—	74[fi]
12	Urea/ChCl	25	4	r.t.	—	91[gi]
13	Urea/ChCl	25	4	r.t.	—	94[hi]
14	Urea/ChCl	20	4	r.t.	—	94[hi]
15	Urea/ChCl	15	4	r.t.	—	94[hi]
16	Urea/ChCl	10	4	r.t.	—	79[hi]
17	Urea/ChCl	15	3	r.t.	—	94[hi]
18	Urea/ChCl	15	1	r.t.	—	94[hi]
19	Urea/ChCl	15	0.5	r.t.	—	61[hi]
20	Urea/ChCl	15	1	r.t.	—	NR[hij]
21	Urea/ChCl	15	1	r.t.	—	NR[ii]
22	Urea/ChCl	15	1	r.t.	—	91[hijk]

[a] Isolated yield. [b] X = NaCl, NaBr, electrolyte. [c] (30%). [d] (50%). [e] Fe rod. [f] Fe foam. [g] Pt rod. [h] oxC$_{60}$–Ly@Fe GCE. [i] Graphite rod. [j] N_2 gas. [k] H_2O (0.5 cc).

weakens the S–Cl bond and promotes stepwise departure of chloride anion radical ($Cl^{-\bullet}$), while concomitant S–O bond formation progressively increases the oxidation state of sulfur. Iterative sequences of "oxygen attack → S–O bond formation → S–Cl bond cleavage convert the initial sulfane chloride species (S–Cl type fragments) into higher-valent sulfur oxo intermediates (sulfenyl, sulfinyl, and sulfonyl species), which are ultimately oxidized to sulfate (SO_3H) under the anodic conditions. This stepwise dechlorination–oxidation sequence is fully consistent with established multi-step radical mechanisms reported for the electrochemical and aerobic oxidation of reduced sulfur species to sulfate.[45]

The interaction between the reactants and the oxC$_{60}$–Ly@Fe GCE catalyst was investigated using density functional theory, with the mechanistic sequence depicted in Fig. 18. Chlorobenzene residing in the interstitial pores of oxC$_{60}$–Ly@Fe reacts with Fe NPs, surmounting an energy barrier of 11.3 kcal mol^{-1} to form the intermediate trichloro(phenyl)-λ^4-sulfane. In parallel, S_8 engages with Cl_2 to generate the intermediate hypochlorous thioanhydride after crossing a barrier of 7.3 kcal mol^{-1}. Subsequent coupling of these intermediates, followed by a nucleophilic attack of hypochlorous thioanhydride on phenyliron(III) chloride, requires overcoming a barrier of 13.5 kcal mol^{-1} to yield trichloro(phenyl)-λ^4-sulfane. Coordination of the Fe NPs to atmospheric oxygen weakens the C–C bond and facilitates the reaction with O_2, promoting oxidation and culminating in the formation of benzenesulfonic acid with a reaction free energy change of 19.6 kcal mol^{-1}. This sequence highlights the roles of the NPs Fe sites in activating substrates, mediating radical and polar steps, and directing the oxidation to the sulfonic acid product.[46]

The SEM and performance data for oxC$_{60}$–Ly@Fe after 10 catalytic cycles indicate a clear deterioration in recyclability. The reuse test shows the catalyst yield dropping from 94% in the initial run to 82% after ten cycles, representing a substantial loss of activity over time (Fig. 19a). The accompanying SEM analysis (Fig. 19b) reveals pronounced morphological changes particle aggregation and notable pore blockage, with exposed surfaces becoming more irregular and many micro- and mesopores appearing clogged by deposition products. This morphological

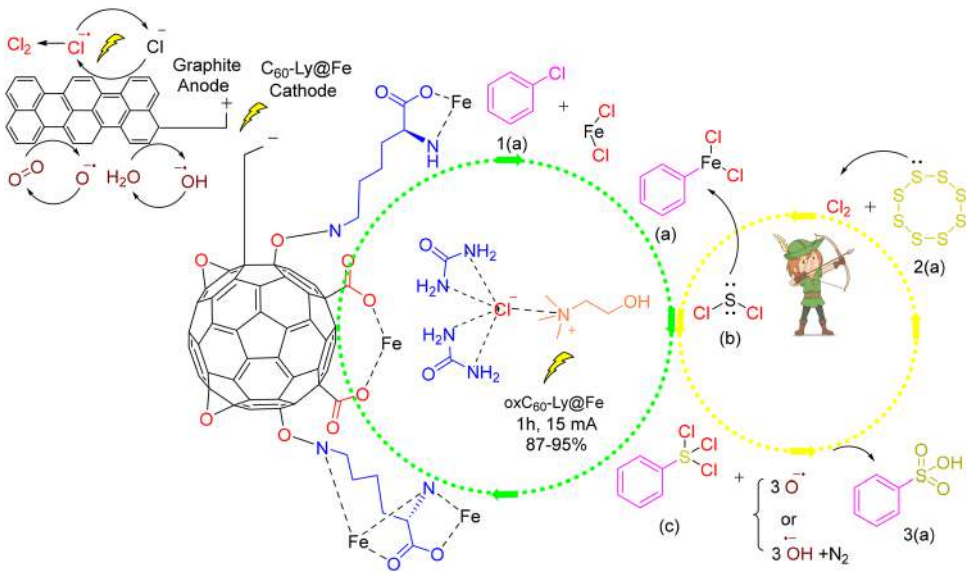


Fig. 17 Reaction mechanism for electro-synthesis of benzenesulfonic acids **3(a–p)**.

 This journal is © The Royal Society of Chemistry and the Centre National de la Recherche Scientifique 2026

Published on 22 January 2026. Downloaded by University of California - Los Angeles on 1/28/2026 4:59:03 PM.

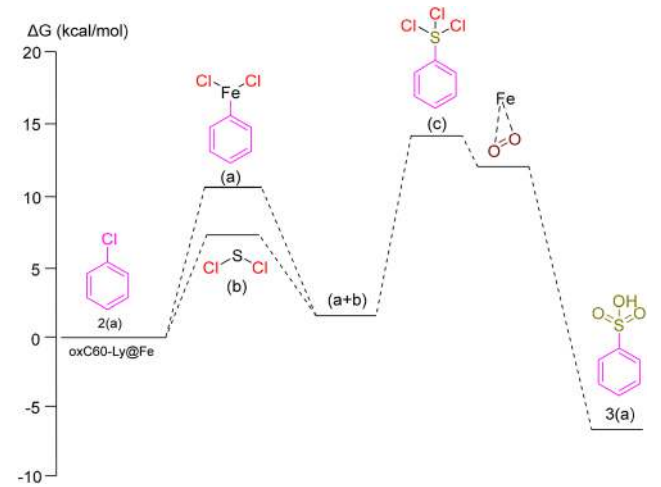


Fig. 18 Comparative thermodynamic analysis of the oxC$_{60}$–Ly@Fe GCE electrocatalytic setup and starting materials.

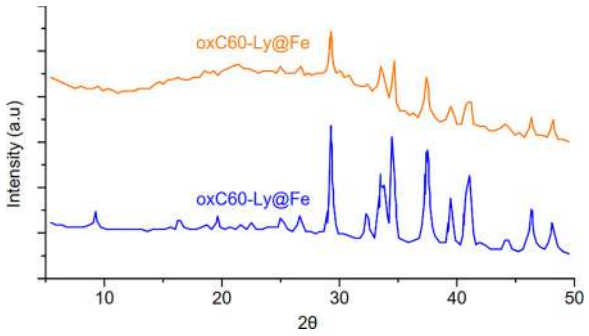


Fig. 20 XRD analysis of fresh and after 10 runs of oxC$_{60}$–Ly@Fe.

evolution provides a mechanistic basis for performance decay, as blocked active sites and altered transport pathways reduce accessible surface area and hinder diffusion of reactants to the active sites.

The XRD patterns of the fresh oxC$_{60}$–Ly@Fe catalyst (Fig. 20, blue curve) and the reused catalyst after 10 consecutive reaction cycles (Fig. 20, orange curve) reveal noticeable structural changes that explain the decline in catalytic performance from 94% to 82% yield. In the fresh sample, well-defined and sharp diffraction peaks are observed, indicating a high degree of crystallinity and a stable arrangement of iron-containing active sites supported on the oxidized fullerene framework. After 10 cycles, the intensity of these characteristic peaks is significantly reduced and partially broadened, suggesting a loss of crystallinity and partial structural disorder within the catalyst (Table 4).

The nitrogen adsorption–desorption isotherm of oxC$_{60}$–Ly@Fe after 10 catalytic cycles (Fig. 21) clearly demonstrates significant textural degradation compared to the fresh catalyst. While the original material exhibited a mesoporous structure with a BET surface area of 351.7 m^2 g^{-1}, pore volume of 0.29 cm^3 g^{-1}, and an average pore diameter of 3.4 nm, after 10 reuse cycles these values drastically decreased to 118.5 m^2 g^{-1}, 0.05 cm^3 g^{-1}, and 1.7 nm, respectively, as shown in Table 5. This substantial reduction in surface area and pore volume indicates partial pore collapse and blockage, likely due to deposition of reaction byproducts, accumulation of sulfur- and chlorine-containing residues within the pore channels during repeated catalytic cycles.

Fig. 22 provides a comprehensive assessment of the stability and durability of the oxC$_{60}$–Ly@Fe GCE electrode under operational electrochemical conditions, specifically utilizing cycling durability and leaching analyses to support the evaluation of its scalability for advanced applications. Panel A presents the results of the cycling durability test, wherein the electrode maintains a stable current density (J) of 15 mA cm^{-2} over a 50-hour period. This consistency in current output confirms the electrode's exceptional electrochemical durability, with no appreciable decline in performance throughout prolonged operation. The maintenance of constant current density serves as evidence for the sustained catalytic activity and structural integrity of the oxC$_{60}$–Ly@Fe GCE, underscoring its suitability for long-term or large-scale application scenarios.

Panel B illustrates the outcomes of the leaching analysis, performed *via* ICP-OES, which tracks the percentage of Fe% present in the reaction solution across varying durations. The

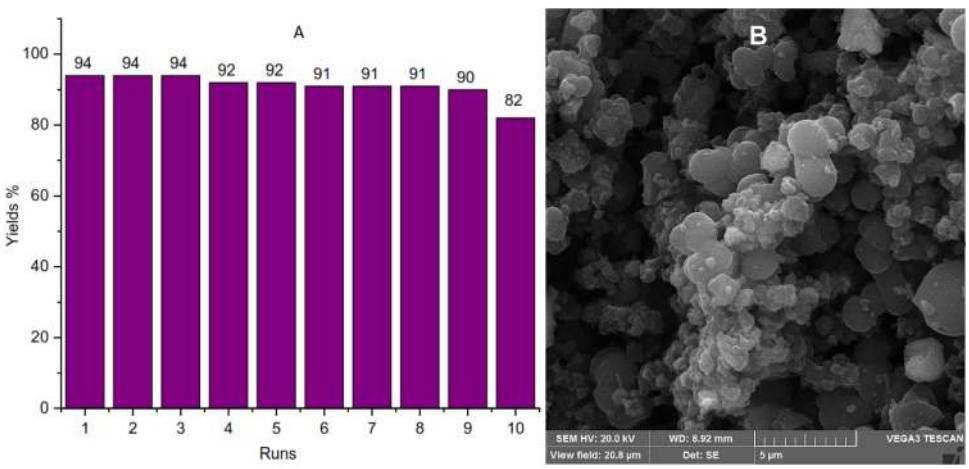
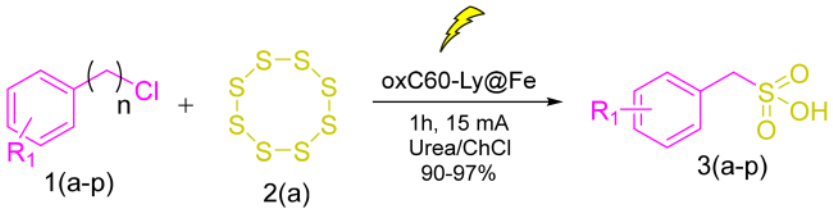


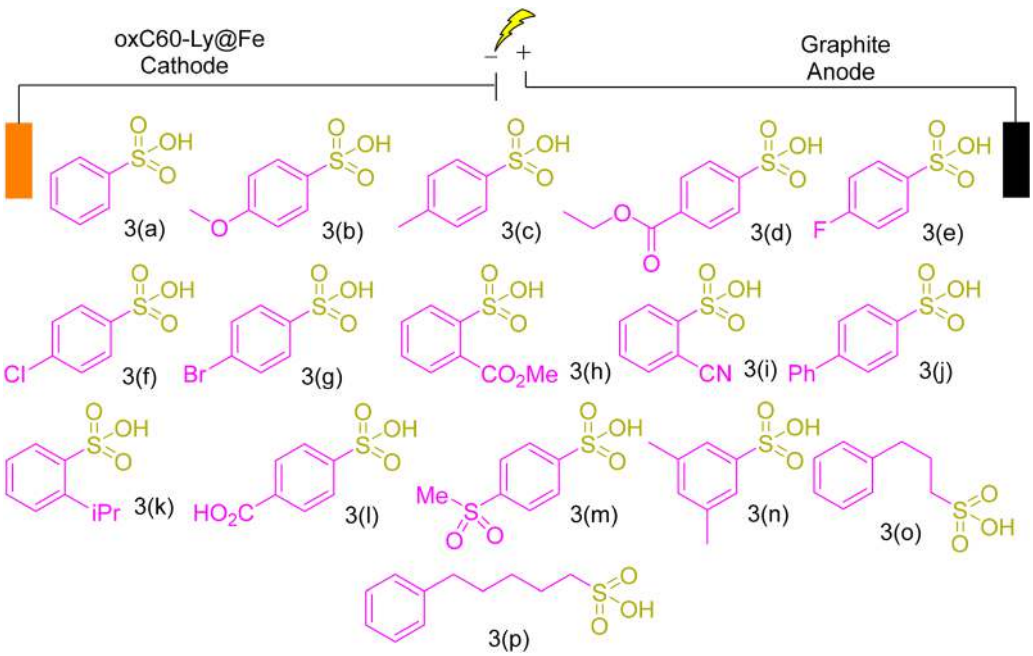
Fig. 19 (a) Reusability test and (b) SEM analysis of oxC$_{60}$–Ly@Fe after 10 runs.

Published on 22 January 2026. Downloaded by University of California - Los Angeles on 1/28/2026 4:59:03 PM.

Table 4 Electro-organic system for synthesis of Benzenesulfonic acids **3(a–p)**



Product	R_1	*n*	M.p. (°C) lit	M.p. (°C)	Yield[a] (%)	*E*/*f*[bc]	*A*/*e*[d]	TON[e]	TOF[f] (min^{-1})
3a	H	0	45–49[19]	47–50	94	0.07	82	211	3.5
3b	4OMe	0	83–85[40]	82–84	97	0.03	84	177	2.95
3c	4Me	0	99–103[19]	100–102	95	0.05	83	194	3.2
3d	$4CO_2Et$	0	—	68–70	92	0.09	87	145	2.4
3e	4F	0	89–92[40]	90–93	91	0.1	84	189	3.1
3f	4Cl	0	95[41]	94–96	95	0.06	85	173	2.88
3g	4Br	0	91–94[40]	93–94	95	0.06	84	141	2.35
3h	$2CO_2Me$	0	—	64–66	92	0.09	86	154	2.56
3i	2CN	0	—	120–123	91	0.11	84	182	3
3j	4Ph	0	134–136[42]	132–134	94	0.11	87	142	2.3
3k	2iPr	0	—	108–110	90	0.11	85	166	2.76
3l	$2CO_2H$	0	68–69[43]	68–71	92	0.09	86	165	2.75
3m	4SMe	0	—	126–127	93	0.07	88	171	2.72
3n	3,5diMe	0	—	122–125	91	0.08	86	175	2.65
3o	H	3	—	101–105	92	0.1	84	177	2.68
3p	H	5	—	99–102	94	0.09	83	168	2.57



[a] Isolated yield. [b] The reaction conditions involved dissolving chlorobenzenes **1(a–p)** and S_8 **2(a)** in 15 mL of urea/ChCl DES. Electrolysis was performed in an undivided cell equipped with graphite and oxC_{60}–Ly@Fe GCE electrodes. A constant current of 15 mA was applied for 1 hour throughout the reaction. [c] *E* factor. [d] Atom economy. [e] TON. [f] TOF.

data reveal a gradual rise in Fe concentration from 2% at 10 hours to 13% at 35 hours, indicative of a controlled but progressive leaching of Fe ions from the electrode material. Such metal leaching is a notable contributor to performance degradation and parallels the observed reduction in reaction yield from 94% to 82%. This underscores the critical importance of leaching analyses for uncovering the underlying causes of efficiency loss and for evaluating the long-term stability and potential recyclability of the electrode during scale-up investigations.

In summary, these results collectively indicate that while the oxC_{60}–Ly@Fe GCE electrode demonstrates strong current stability during extended cycling; however, gradual Fe leaching and structural alterations diminish its long-term catalytic efficiency. After recycling, the material undergoes a transition from a mesoporous to a predominantly microporous structure, which restricts mass transfer and reduces access to active sites. These structural changes together with Fe species aggregation or loss, surface oxidation, and partial blockage of active sites by

 This journal is © The Royal Society of Chemistry and the Centre National de la Recherche Scientifique 2026

Published on 22 January 2026. Downloaded by University of California - Los Angeles on 1/28/2026 4:59:03 PM.

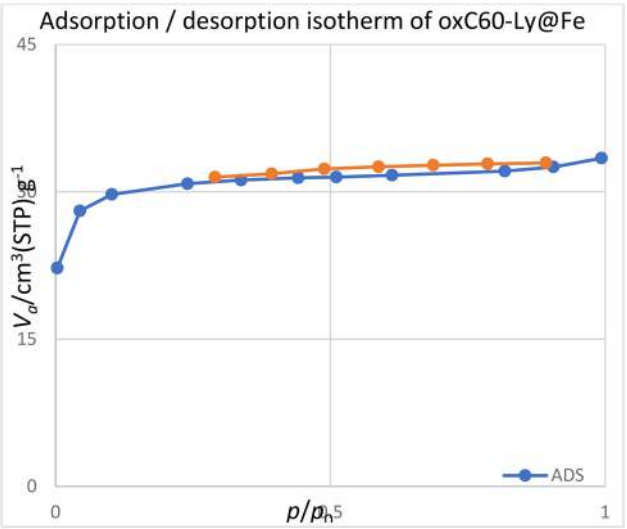


Fig. 21 BET analysis of oxC$_{60}$–Ly@Fe after 10 runs.

Table 5 BET analysis of oxC$_{60}$–Ly@Fe after 10 runs

Sample	BET surface area [m^2 g^{-1}]	Pore volume [cm^3 g^{-1}]	Average pore diameter [nm]	Type of pore
oxC$_{60}$–Ly@Fe	118.5	0.05	1.7	Microporous

reaction residues contribute to the decline in catalytic efficiency from 94% to 82% after 10 cycles. XRD analysis also reveals slight peak shifts indicative of minor structural strain and ongoing deterioration of the catalyst framework. Additional factors, including pore fouling, framework restructuring or sintering, ligand degradation, and the formation of surface oxides or carbonaceous deposits, further limit the number of accessible active sites and progressively compromise catalytic performance during repeated cycling.

Table 6 presents a detailed practical and comparative analysis of electro-organic sulfonation reactions. In 2018, Yong *et al.* reported an 88% yield for the electro-sulfonation reaction using a Ni electrode in MeCN solvent, with a current of 12 mA applied for 3 hours at room temperature (Table 6, entry 1). Subsequently, Han and Zhan independently reported yields of 75% and 76%, respectively, in 2019 using Pt electrodes in DMSO and MeCN solvents, applying currents of 5 and 10 mA for reaction times of 10 and 4.5 hours under ambient conditions (Table 6, entries 2 and 3). In 2020, Yin and Yavari *et al.* achieved yields of 81% and 82%, respectively, employing Pt and stainless-steel electrodes in H_2O and MeOH solvents at 40 mA current, with 3 and 10 hours reaction times at room temperature (Table 6, entries 4 and 5). Yu and Ming, in 2021, reported yields of 66% and 77% using Pt electrodes in MeCN solvent, operating under currents of 5 and 2 mA for 6 and 10 hours at ambient conditions (Table 6, entries 6 and 7). Collectively, these studies highlight limitations such as prolonged reaction times, the use of expensive electrodes impeding commercial scalability, moderate yields, and reliance on hazardous reagents. In contrast, the electrocatalytic system developed in this work, utilizing a cost-effective, environmentally benign, and reusable oxC$_{60}$–Ly@Fe GCE electrode in conjunction with a recyclable urea/ChCl DES electrolyte, demonstrated enhanced performance with a 94% yield at 15 mA current, 1-hour reaction time, and ambient temperature (Table 6, entry 8). This advancement underscores the improved commercial feasibility and robust catalytic efficiency of the proposed method.

Conclusion and outlook

In conclusion, the development of the sustainable and recyclable oxC$_{60}$–Ly@Fe GCE electrode offers a highly eco-friendly catalytic platform for the electrochemical sulfonation of benzenesulfonic acid derivatives. This catalyst effectively overcomes the drawbacks of traditional sulfonation methods, providing mild reaction conditions, high product yields (90–97%), and excellent adherence to green chemistry principles as evidenced by favorable *E*-factor, atom economy, TON, and TOF values. Comprehensive physicochemical characterizations confirm the catalyst's structural integrity and functionality, while detailed

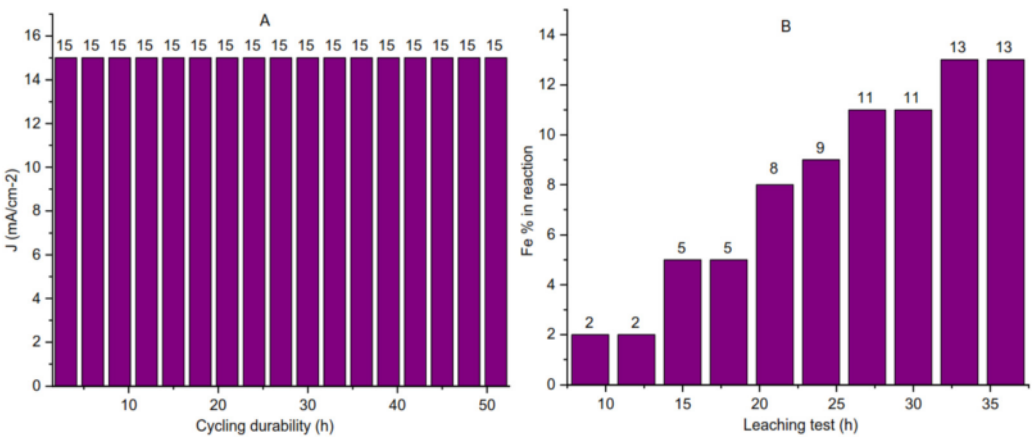


Fig. 22 (a) Cycling durability and (b) leaching test of oxC$_{60}$–Ly@Fe GCE.

Published on 22 January 2026. Downloaded by University of California - Los Angeles on 1/28/2026 4:59:03 PM.

Table 6 Comparative investigation of electro-organic synthetic routes to sulfonic derivatives

Entry	Electrolyte and reagent	Electrode	Catalyst	Solvent	Conditions	Year	Yield (%)
1	Bu_4NBF_4	C/Ni	Ni	MeCN	12 mA, 3 h, r.t.	2018	88[17]
2	Bu_4NBF_4	C/Pt	Pt	DMSO	5 mA, 10 h, r.t.	2019	75[47]
3	Bu_4NBF_4	C/Pt	Pt	MeCN	10 mA,4.5 h, r.t.	2019	76[48]
4	Bu_4NI	Pt/Pt	Pt	H_2O	40 mA, 3 h, r.t.	2020	81[49]
5	KI	PG/St	St	MeOH	40 mA, 10 h, r.t.	2020	82[50]
6	Bu_4NBF_4	C/Pt	Pt	MeCN	5 mA, 6 h, r.t.	2021	66[51]
7	Bu_4NBF_4	C/Pt	Pt	MeCN	2 mA, 10 h, r.t.	2021	77[52]
8	Urea/ChCl	C/Fe	Fe	—	15 mA, 1 h, r.t.	This work	94

analyses of the sulfonic acid derivatives validate the success of the electro-synthetic methodology.

Looking forward, this electrocatalytic approach holds great promise for scalable industrial applications, enabling sustainable production of sulfonated aromatic compounds. Further exploration of the catalyst's mechanistic pathways and extension to broader substrate scopes may enhance its versatility and efficiency, contributing to the advancement of greener and more sustainable synthetic methods in organic chemistry. The catalyst also exhibits chirality, enabling its application in enantioselective reactions. also, its chiral nature presents opportunities for detailed investigation of stereoselective catalytic performance and the potential for commercial development in asymmetric synthesis.

Author contributions

Karkaz Thalij: investigation; methodology. Ebraheem Abdu Musad Saleh: investigation; supervision; writing – original draft. Amer Alhaj Zen: visualization; project administration. Mohammed B. Alqaraguly: data curation; writing – original draft. Abdulrahman A. Almehizia: conceptualization; software; funding acquisition. Erkabay Eshchanov: methodology; software; investigation. Bekzod. Madaminov: investigation; methodology. Zokir Ataullaev: investigation; methodology. Yuldash Rajabovich Takhirov: formal analysis; resources; writing – review & editing. Elyor Berdimurodov: investigation; validation. Khasan Berdimuradov: software; visualization. Rasulbek Eshmetov: investigation; methodology.

Conflicts of interest

The authors declare that they have no known competing financial interests or personal relationships that could have appeared to influence the work reported in this paper.

Data availability

Data underpinning the findings of this study can be accessed by contacting the corresponding author upon making a reasonable request.

Acknowledgements

The authors are grateful to King Saud University, Riyadh, Saudi Arabia, for funding this work through the Ongoing Research Funding program—Research Chairs (ORF-RC-2025-0116). The authors extend their thanks for support to Urgench State University named after Abu Rayhan Biruni, Urgench city

References

1 B. Han, X. Ding, Y. Zhang, X. Gu, Y. Qi and S. Liang, Mn (OAc) 3-Promoted Sulfonation–Cyclization Cascade via the SO3–Radical: The Synthesis of Heterocyclic Sulfonates, *Org. Lett.*, 2022, **24**, 8255–8260.
2 K. Kurogi, M. Suiko and Y. Sakakibara, Evolution and multiple functions of sulfonation and cytosolic sulfotransferases across species, *Biosci., Biotechnol., Biochem.*, 2024, **88**, 368–380.
3 A. Akram, M. Iqbal, A. Yasin, K. Zhang and J. Li, Sulfonated molecules and their latest applications in the field of biomaterials: a review, *Coatings*, 2024, **14**, 243.
4 A. Korkmaz and E. Bursal, Synthesis, characterization, biological evaluation, ADMET, and molecular docking studies of novel chalcone-sulfonate hybrid compounds as potential antioxidant and antiobesity activities, *J. Mol. Struct.*, 2025, **1332**, 141638.
5 S. K. Zyryanov and E. A. Baybulatova, Current challenges for therapy of comorbid patients: a new look at celecoxib. A review, *Ter. Arkh.*, 2024, **96**, 531–542.
6 S. M. Gupta, A. Behera and S. Singh, Pharmacological Potential of Sulindac and Its Active Metabolite: A Comprehensive Review, *Curr. Drug Ther.*, 2024, **19**, 765–779.
7 X. Wang, S. Shu, Y. Wang and X. Zeng, Degradation of Sulfathiazole by Heat-Activated Persulfate: Kinetics, Degradation Pathways, and Toxicity Assessment, *J. Environ. Eng.*, 2025, **151**, 04025019.
8 V. Domingos, K. Nezvalova-Henriksen, A. Dadkhah, M.-E. Moreno-Martinez, K. Ben Hassine, V. Pires, N. Kröger, T. Bauters, M. Hassan and N. Duncan, A practical guide to therapeutic drug monitoring in busulfan: recommendations from the Pharmacist Committee of the European Society for Blood and Marrow Transplantation (EBMT), *Bone Marrow Transplant.*, 2024, **59**, 1641–1653.
9 H. Zheng, Y. Zhang, S. Li, X. Feng, Q. Wu, Y. K. Leong and J.-S. Chang, Antibiotic sulfadiazine degradation by persulfate oxidation: Intermediates dependence of ecotoxicity and the induction of antibiotic resistance genes, *Bioresour. Technol.*, 2023, **368**, 128306.
10 K. Donoghue, L. Hermann, E. Brobbin and C. Drummond, The rates and measurement of adherence to acamprosate in

 This journal is © The Royal Society of Chemistry and the Centre National de la Recherche Scientifique 2026

Published on 22 January 2026. Downloaded by University of California - Los Angeles on 1/28/2026 4:59:03 PM.

randomised controlled clinical trials: a systematic review, *PLoS One*, 2022, **17**, e0263350.

11 R. L. Araújo, J. X. L. Neto, U. L. Fulco, J. I. N. Oliveira, M. L. Lyra and V. Manzoni, DFT investigation of the solid-state properties and Hirshfeld surface analysis of antidiabetic drugs: acetohexamide and Tolazamide, *Chem. Phys. Lett.*, 2023, **833**, 140934.

12 A. Nasrullaev, K. Bozorov, K. Bobakulov, J. Zhao, L. F. Nie, K. K. Turgunov, B. Elmuradov and H. A. Aisa, Synthesis, characterization, and antimicrobial activity of novel hydrazone-bearing tricyclic quinazolines, *Res. Chem. Intermed.*, 2019, **45**, 2287–2300.

13 J. S. Chauhan and R. Gajre, Analytical method development and validation for Estimation of Calcium Dobesilate and Docusate Sodium in Pharmaceutical dosage form with QbD approach, *Res. J. Pharm. Dosage Forms Technol.*, 2021, **13**, 213–229.

14 Y. Zeng, L. Nie, L. Liu, C. Niu, Y. Li, K. Bozorov, J. Zhao, J. Shen and H. A. Aisa, Design, synthesis, in vitro evaluation of a new pyrrolo[1,2-*a*]thiazolo[5,4-*d*]pyrimidinone derivatives as cholinesterase inhibitors against Alzheimer's disease, *J. Heterocycl. Chem.*, 2022, **59**, 1086–1101.

15 C. Chu, Y. Liu, M. Mao, D. Wang, J. Liu, H. Wei, M. Yu and J. Cai, Synthesis of 1,3,4-thiadiazoles from elemental sulfur via three-component cyclization under metal-free conditions, *Org. Biomol. Chem.*, 2025, **23**, 5101–5105.

16 T. Lu, L. Nie, D. Tang, K. Bozorov, J. Zhao and H. A. Aisa, Synthesis of tricyclic pyrazolopyrimidine arylidene ester derivatives and their cytotoxic and molecular docking evaluations, *J. Heterocycl. Chem.*, 2024, **61**, 651–668.

17 Y. Yuan, Y. Cao, Y. Lin, Y. Li, Z. Huang and A. Lei, Electrochemical oxidative alkoxysulfonylation of alkenes using sulfonyl hydrazines and alcohols with hydrogen evolution, *ACS Catal.*, 2018, **8**, 10871–10875.

18 A. R. Moosavi-Zare, M. A. Zolfigol and E. Noroozizadeh, Regioselective sulfonation of aromatic compounds over 1,3-disulfonic acid imidazolium chloride under aqueous media, *Synlett*, 2016, 1682–1684.

19 A. R. Hajipour, B. B. F. Mirjalili, A. Zarei, L. Khazdooz and A. E. Ruoho, A novel method for sulfonation of aromatic rings with silica sulfuric acid, *Tetrahedron Lett.*, 2004, **45**, 6607–6609.

20 A. W. Ruttinger, *Development of Energy Systems Towards a Low Carbon Future: From Atoms to Policies*, Cornell University, 2021.

21 K.-T. Lee and C.-Y. Pien, Preparation of monosodium 2-sulfoterephthalate to make a MIL-101 (Cr)–SO_3H catalyst, *New J. Chem.*, 2022, **46**, 868–876.

22 A. Khazaei, M. A. Zolfigol, A. R. Moosavi-Zare, J. Afsar, A. Zare, V. Khakyzadeh and M. H. Beyzavi, Synthesis of hexahydroquinolines using the new ionic liquid sulfonic acid functionalized pyridinium chloride as a catalyst, *Chin. J. Catal.*, 2013, **34**, 1936–1944.

23 S. Y. Kalurazi, K. Rad-Moghadam and S. Moradi, Efficient catalytic application of a binary ionic liquid mixture in the synthesis of novel spiro [4*H*-pyridine-oxindoles], *New J. Chem.*, 2017, **41**, 10291–10298.

24 K. Cen, Y. Liu, J. Yu, Z. Zeng, Q. Hou, G. He, M. Ouyang, Q. Wang, D. Wang and F. Zhao, Electrocatalytic cascade selenylation/cyclization/deamination of 2-hydroxyaryl enaminones: Synthesis of 3-selenylated chromones under mild conditions, The, *J. Org. Chem.*, 2024, **89**, 8632–8640.

25 Z. Zeng, F. Zhao, H. Zhong, Z. Yang, H. Wei, S. Ji, M. Yu and J. Cai, Electrochemical Synthesis of 3,5-Disubstituted Pyrazoles from Ynone Hydrazones via Diselenide-Catalyzed Cyclization Strategy, *J. Org. Chem.*, 2025, **90**, 15345–15356.

26 J. Sato, M. Fujita, N. Shida and M. Atobe, Electrochemical Amide Bond Formation via Chemoselective Oxidation of Hemiaminals with Gold Electrocatalyst, *ACS Electrochem.*, 2024, **1**, 45–51.

27 Y. F. Zhang, E. Schulz and M. Mellah, Electrocatalytic, Sm-Promoted Synthesis of Aminoarenes from Nitroaromatic Derivatives in MeOH, *ChemCatChem*, 2024, **16**, e202400303.

28 Z. Zhang, W. Yang, C. Liu, X. Yu, S. Song and C. Xia, Tandem Electrochemical Redox/Condensation Reaction Between 2-Amino Nitrobenzenes and Aliphatic Alcohols: An Approach to Benzimidazoles, *Adv. Synth. Catal.*, 2024, **366**, 4667–4673.

29 K. T. Nguyen, M. Sukwattanasinitt and S. Wacharasindhu, Electrosynthesis of benzimidazole-fused quinazolinones via a cascade addition–desulfurization–cyclization process, Tetrahedron, *Green Chem.*, 2025, **5**, 100068.

30 A. Ali, D. J. Jasim, N. Rakhimov, M. J. Mohammed, M. M. Karim, A. H. Athab, A. Kumar, N. Ahmad and L. Guo, Development and characterization of an aluminum-enhanced graphene oxide nanocomposite: An Eco-friendly and sustainable catalyst for electrochemical Friedel–Crafts reactions, *J. Mol. Struct.*, 2025, **1319**, 139373.

31 A. Naveed, H. Ai, T. Li, A. Ali, J. M. Moradian, W. A. Qureshi, M. Su, X. Li, Y. Zhou and R. Guo, Two birds with one stone: green solvent enabled high-stability and durable Zn anode in both non-aqueous and aqueous electrolytes, *Adv. Funct. Mater.*, 2024, **34**, 2400949.

32 H. Naz, R. N. Ali, W. A. Qureshi, A. Ali, N. A. Albert and G. Zhu, Boosting oxygen evolution with electrodes composed of metal sulfides and hydrogen bonded organic frameworks, Sustainable, *Energy Fuels*, 2024, **8**, 3174–3181.

33 J. Qi, X. Wang, G. Wang, S. R. Dubbaka, P. O'Neill, H. T. Ang and J. Wu, Sustainable electrocatalytic oxidation of *N*-alkylamides to acyclic imides using H_2O, *Green Chem.*, 2024, **26**, 306–311.

34 A. A. Mohammadi, S. Makarem, R. Ahdenov and N. A. Notash, Green pseudo-multicomponent synthesis of some new spirocyclopropane derivatives via electro-catalyzed reaction, *Mol. Diversity*, 2020, **24**, 763–770.

35 R. Amoroso, F. Hollmann and C. Maccallini, Choline chloride-based DES as solvents/catalysts/chemical donors in pharmaceutical synthesis, *Molecules*, 2021, **26**, 6286.

36 H.-S. Lin, Y. Ma, R. Xiang, S. Manzhos, I. Jeon, S. Maruyama and Y. Matsuo, One-step direct oxidation of fullerene-fused alkoxy ethers to ketones for evaporable fullerene derivatives, Communications, *Chemistry*, 2021, **4**, 74.

37 Z. Behrouz, K. Banihashemi, M. Saadat, S. Alizadeh and R. Ahdenov, Electrode Development for Electro-Organic

Published on 22 January 2026. Downloaded by University of California - Los Angeles on 1/28/2026 4:59:03 PM.

Kolbe–Schmitt C–H Carboxylation of Benzene Using Cu Nanoparticles on Graphene Oxide Modified With MIL-101 MOF for CO_2 Capture in a DES Electrolyte System, *Appl. Organomet. Chem.*, 2025, **39**, e7905.

38 N. C. Deucher, R. Silva de Souza Jr and E. M. Borges, Teaching precipitation Titration methods: a statistical comparison of Mohr, Fajans, and Volhard techniques, *J. Chem. Educ.*, 2024, **102**, 364–371.

39 D. Korkmaz, Precipitation titration:''determination of chloride by the Mohr method'', *Methods*, 2001, **2**, 1–6.

40 L.-L. Zuo, S. Qin, P. Zhang, Y.-J. Qin and Z.-X. Guo, Mechanochemical sulfonation of aromatic compounds using $NaHSO_4$ H_2O/P_2O_5, *J. Chem. Res.*, 2021, **45**, 942–949.

41 L. Hou, M. Zhang, L. Shi, X. Luo, R. De, W. Chen, Y. Jing and Y. Bao, Novel Oxaprozin Cocrystals/Salts: Solubility Enhancement for Oxaprozin and Release Control for Minoxidil, *Cryst. Growth Des.*, 2025, **25**, 3013–3028.

42 S. Qin, P. Zhang, Y.-J. Qin and Z.-X. Guo, Facile synthesis of diarylsulfones from arenes and $3CdSO_4{\cdot}xH_2O$ via mechanochemistry, *Tetrahedron Lett.*, 2020, **61**, 151567.

43 P. Venkata Ramana and A. Ram Reddy, Synthesis of a few cyclothiadiazanones and aminosulfonyl benzamides from saccharin, *J. Sulfur Chem.*, 2010, **31**, 71–81.

44 R. Ahdenov, A. A. Mohammadi, S. Makarem, S. Taheri and H. Mollabagher, Eelectrosynthesis of benzothiazole derivatives via C–H thiolation, *Heterocycl. Commun.*, 2022, **28**, 67–74.

45 X. Xia, F. Zhu, J. Li, H. Yang, L. Wei, Q. Li, J. Jiang, G. Zhang and Q. Zhao, A review study on sulfate-radical-based advanced oxidation processes for domestic/industrial wastewater treatment: degradation, efficiency, and mechanism, *Front. Chem.*, 2020, **8**, 592056.

46 S. Vuckovic, S. Song, J. Kozlowski, E. Sim and K. Burke, Density functional analysis: The theory of density-corrected DFT, *J. Chem. Theory Comput.*, 2019, **15**, 6636–6646.

47 H. S. Kim and S. Lee, Electrochemical Coupling of Arylsulfonyl Hydrazides and Tertiary Amines for the Synthesis of β-Amidovinyl Sulfones, *Eur. J. Org. Chem.*, 2019, 6951–6955.

48 Z. Zhang, J. Yan, D. Ma and J. Sun, Electrochemical synthesis of β-hydroxy-, β-alkoxy-, and β-carbonyloxy sulfones by vicinal difunctionalization of olefins, *Chin. Chem. Lett.*, 2019, **30**, 1509–1511.

49 Y.-L. Lai, Y. Mo, S. Yan, S. Zhang, L. Zhu, J. Luo, H. Guo, J. Cai and J. Liao, Electrochemical sulfonylation of alkenes with sulfonyl hydrazides: a metal-and oxidant-free protocol for the synthesis of (*E*)-vinyl sulfones in water, *RSC Adv.*, 2020, **10**, 33155–33160.

50 I. Yavari and S. Shaabanzadeh, Electrochemical synthesis of β-ketosulfones from switchable starting materials, *Org. Lett.*, 2020, **22**, 464–467.

51 M. Yu, H. Wang, Y. Gao, F. Bu, H. Cong and A. Lei, Manganese-catalyzed chlorosulfonylation of terminal alkene and alkyne via convergent paired electrolysis, *Cell Rep. Phys. Sci.*, 2021, **2**, 100476–100491.

52 M.-M. Zhang, Y. Sun, W.-W. Wang, K.-K. Chen, W.-C. Yang and L. Wang, Electrochemical synthesis of sulfonated benzothiophenes using 2-alkynylthioanisoles and sodium sulfinates, *Org. Biomol. Chem.*, 2021, **19**, 3844–3849.

 This journal is © The Royal Society of Chemistry and the Centre National de la Recherche Scientifique 2026